JOURNAL OF GEOPHYSICAL RESEARCH, VOL. 112, D05201, doi:10.1029/2006JD007555, 2007

Cloud properties and associated radiative heating rates in the tropical western Pacific

James H. Mather,[1] Sally A. McFarlane,[1] Mark A. Miller,[2] and Karen L. Johnson[2]

Received 24 May 2006; revised 20 September 2006; accepted 20 October 2006; published 1 March 2007.

[1] Calculations of radiative flux profiles require measurements of thermodynamic and cloud properties (temperature, humidity, liquid and ice water content). Instruments capable of making these measurements have only recently become available. The U.S. Department of Energy Atmospheric Radiation Measurement (ARM) Program operates a comprehensive set of atmospheric remote sensing instruments at sites around the world, including three in the tropical western Pacific region. We have processed several months of ARM observations from two of these sites, Manus and Nauru, to calculate time series of vertical cloud property profiles and associated radiative fluxes and heating rates. Maxima in cloud occurrence are found in the boundary layer and the upper troposphere at both sites. Manus, which was much more convectively active than Nauru during the study period, also exhibits a midlevel cloud feature near the melting level. The two sites exhibit very different diurnal cycles. Manus experiences an afternoon maximum in high clouds while Nauru experiences a weak afternoon minimum. Nauru experiences a strong afternoon maximum in boundary layer clouds. Calculated fluxes at the surface and the top of the atmosphere are found to be in reasonable agreement with measurements. Below 15 km, radiative processes lead to cooling in the average profile, with local maxima near the surface and approximately 8 km. On average, high and midlevel clouds have a net warming effect though not enough to offset the clear-sky cooling. The prevalent boundary layer clouds at Nauru have a net cooling effect in and above the cloud layer and a net warming below. This data set will be an important tool for describing radiative processes in the tropics and assessing the simulation of these processes in dynamical models.

Citation: Mather, J. H., S. A. McFarlane, M. A. Miller, and K. L. Johnson (2007), Cloud properties and associated radiative heating rates in the tropical western Pacific, *J. Geophys. Res.*, *112*, D05201, doi:10.1029/2006JD007555.

1. Introduction

[2] The radiative balance in the tropical Western Pacific is largely modulated by a complex pattern of cloudiness that includes isolated convective cells, mesoscale convective systems, and outflow from these convective cells at multiple levels [*Houze*, 1989; *Johnson et al.*, 1999]. The local radiative heating rate profile is determined by the location, composition, and fractional coverage of the region's diverse cloud configurations. Shallow cumulus fields and high clouds, for example, have a strong cooling effect on the surface through the reflection of shortwave radiation [*Larson et al.*, 1999; *Tian and Ramanathan*, 2002].

[3] The net radiative heating of the atmospheric column can be deduced from radiation measurements at the surface and from satellites. While the net radiative heating of the atmospheric column represents the radiative heat source in the atmospheric energy budget, it is also important, though much more difficult, to describe the vertical distribution of the radiative heating. The vertical distribution of radiative heating influences the local cloud structure and large-scale tropical circulations. Model simulations of tropical anvils, which tend to be widespread in the tropics, show that they heat the upper troposphere [*Ackerman et al.*, 1988]. This net radiative heating can result in widespread destabilization and vertical lifting [*Ackerman et al.*, 1988; *Gu and Liou*, 2000]. Large-scale tropical dynamics may also be driven by the destabilizing effects of infrared cooling associated with water vapor or by differential heating between clear and cloudy regions [*Zhang and Chou*, 1999; *Grabowski and Moncrieff*, 2002]. Failure to properly account for these effects in models may account for the difficulty in simulating important tropical circulations, such as the Madden-Julian Oscillation (MJO) [*Lin et al.*, 2004].

[4] Regional profiles of radiative heating rates can be derived as a residual of diabatic processes computed from radiosonde profiles and surface measurements [*Johnson and Ciesielski*, 2000; *Ciesielski et al.*, 2003]. Radiative fluxes and accompanying heating rates may be computed more directly from profiles of the temperature, humidity, condensed water content, cloud particle size distributions, and

[1]Pacific Northwest National Laboratory, Richland, Washington, USA.
[2]Brookhaven National Laboratory, Upton, New York, USA.

0148-0227/07/2006JD007555$09.00

cloud fractional coverage. Profiles of water vapor and cloud properties are challenging to obtain in the data sparse tropics and several approaches have been used. Several studies use satellite observations to obtain the necessary cloud properties for calculating radiative heating rates [*Sohn*, 1999; *Bergman and Hendon*, 1998; *Ramsey and Vincent*, 1995]. A common source of satellite-derived spatial cloud information for radiative studies is the International Satellite Cloud Climatology Project (ISCCP [*Rossow and Schiffer*, 1991, 1999]). ISCCP has been a valuable source of global cloud distributions; however, it relies on passive sensors which provide limited information about vertical structure [*Zhang et al.*, 2004].

[5] An early estimate of cloud properties and radiative heating rate profiles using active remote sensors in the tropical Atlantic was computed from cloud fields derived from a combination of satellite, surface radar, and aircraft data during the Global Atmospheric Research Program (GARP) Atlantic Tropical Experiment (GATE) [*Cox and Griffith*, 1979a, 1979b]. *Qian* [2003] applied a similar approach for the Tropical Ocean Global Atmosphere Coupled Ocean Atmospheric Response Experiment (TOGA COARE) using radiosonde profiles combined with satellite and ground-based cloud lidar observations. These estimates are widely used despite the relatively short duration of these experiments and the relatively coarse resolution of the retrieved cloud structure.

[6] More sophisticated surface-based remote sensing techniques are enabling increasingly detailed measurements of cloud properties, which can be used to compute heating rates. *Jensen et al.* [2002] used a combination of millimeter and centimeter wavelength radars to determine vertical profiles of cloud properties during the Maritime Continent Thunderstorm Experiment (MCTEX). Millimeter wavelength radars, which are typically vertically pointing, are excellent tools for observing cloud profiles because they are sensitive to most cloud particles and are only weakly attenuated by cloud liquid water. The scanning centimeter wavelength radar in the work by *Jensen et al.* [2002] was used to provide additional spatial information and to account for attenuation due to precipitation. This study showed the potential of millimeter radars in the tropics but the data were only available during the limited period of the experiment.

[7] The U.S. Department of Energy Atmospheric Radiation Measurement (ARM) Program operates cloud and radiation measurement sites on the islands of Manus (2.06°S, 147.42°E) and Nauru (0.52°S, 166.92°E) as well as in Darwin, Australia (12.42°S, 130.89°E) in the Tropical Western Pacific (TWP) region [*Mather et al.*, 1998]. Data from the ARM sites in the TWP present a unique opportunity to estimate radiative flux and heating rate profiles. They provide cloud properties at unprecedented vertical and temporal resolution comparable to the temporal and spatial scales of clouds located in the column. While these profiles are specific to the columns above the ARM sites, *Jakob and Tselioudis* [2003] show that cloud systems over the ARM TWP sites are typical of the larger western Pacific region. In this study, radar data are used in combination with measurements from passive sensors to calculate vertical profiles of cloud properties and radiative heating. Several months of observations are examined from Manus (February to July 2000) and Nauru (March to December 1999). The intent of this study is to describe the procedure for calculating these profiles from ARM measurements (sections 2 to 4), to describe some of the features in the cloud and radiative heating profiles (section 5), and to evaluate the heating rates through sensitivity tests (section 6).

2. Data

[8] ARM TWP measurements used in this study include temperature and humidity profiles from twice-daily radiosonde launches, broadband surface radiative fluxes, and surface air temperature. Microwave radiometers (MWRs) provide measurements of column integrated water vapor and liquid. These sites also include active remote sensing instruments: millimeter wavelength cloud radar (MMCR), Micropulse lidar (MPL) and ceilometers which provide vertical distributions of hydrometeors. ARM has been collecting MMCR data at Nauru since the site's installation (in November 1998) and at Manus since 1999.

[9] Profiles of temperature, water vapor, and cloud properties are required to calculate the radiative flux profiles. Radiosondes are the primary means of obtaining the vertical distribution of temperature and water vapor at the tropical ARM sites. Radiosondes are launched at nominally 12-hour intervals (0000 and 1200 UTC), which is a much coarser time resolution than the profiles provided by the MMCR and other active remote sensors. Cloud properties vary more rapidly than the water vapor profile, but water vapor can change significantly over the 12 hours between radiosonde launches. Changes in column water vapor and surface layer temperature between radiosonde launches are constrained using 1-min resolution surface temperature data and the 20-s water vapor time series from a 2-channel (23.8, 31.4 GHZ) MWR [*Westwater*, 1993]. Details of the interpolation procedure are given in Appendix A.

[10] Temperature profiles from the radiosondes are used up to 21 km in the radiative transfer calculations. Above this height, the constructed temperature profile is blended with the temperature profile from a standard tropical atmosphere using a weighting function approach. The radiosonde hygrometer measurements become significantly less accurate with height [*Sapucci et al.*, 2005] as the water vapor concentrations decrease. Above 100 hPa a constant mixing ratio with height is assumed. The ozone vertical mixing ratio profile from the standard tropical atmosphere is used throughout the column. Average temperature and relative humidity profiles for Manus are shown in Figure 1.

[11] Cloud location and microphysical profiles are derived primarily from the MMCR, which is a vertically pointing Doppler radar operating at 34.86 GHz. The MMCR is sensitive to hydrometeors, including cloud droplets and precipitation. The MMCR cycles between four operational modes (general, boundary layer, cirrus, and precipitation) over a period of 40 s. Its sensitivity at 5 km ranges from −32 dBZ to −48 dBZ [*Clothiaux et al.*, 1999]. Data from the four modes are merged together with lidar and ceilometer cloud base information by an algorithm known as the Active Remote Sensing of Cloud Layers (ARSCL [*Clothiaux et al.*, 2000]), The output of ARSCL is a best estimate of hydrometeor reflectivity and cloud base height at 10-s temporal and 45-m vertical resolution.

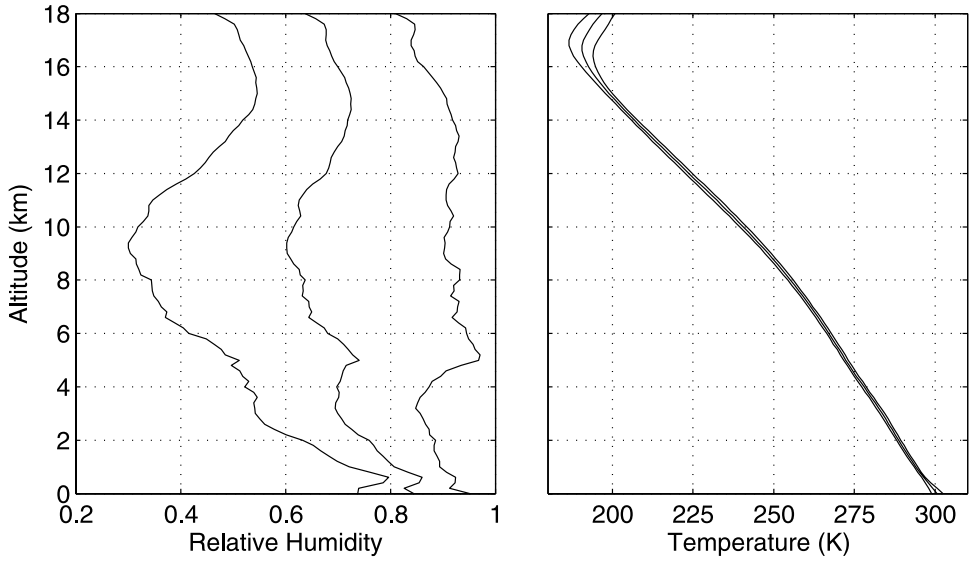

Figure 1. Relative humidity (with respect to ice for T < 0°C) and temperature profiles observed at Manus. The center traces are the average profiles while the standard deviation of each parameter has been added and subtracted from the average to produce the outer curves. The relative humidity profiles show moist layers near 0.5 km, 5 km, and 15 km. The first two layers correspond to the top of the boundary layer and the melting level respectively.

[12] The effective radar reflectivity factor, as reported in the ARSCL product, is the basis for determining profiles of cloud water content. Because of radar limitations, profiles containing precipitating clouds are removed for the purpose of heating rate calculations. A precipitating cloud is defined as one occurring in a column with radar reflectivity > 0 dBZ below 4 km or surface precipitation > 0.1 mm/hr (as measured by a surface rain gauge). This definition of precipitating clouds removes 13.1% of the Manus profiles and 2.8% of the Nauru profiles. Additionally, the MMCR may be sensitive to drizzle or virga below cloud base, which is not radiatively important, so a laser-based estimate of cloud base height is used in these cases. Cases where virga is removed, but the first two tests are passed, are processed with the virga layer defined to be a clear region.

[13] The MMCR also has difficulty detecting high, thin cirrus clouds consisting of small ice crystals. At Nauru, previous studies found that the MMCR fails to detect cirrus with base heights greater than 15 km, which correspond to 13% of the cirrus detected by the MPL [*Comstock et al.*, 2002]. These high cirrus clouds are generally optically thin, with a mean optical depth of only 0.04. They have little effect on the surface radiative budget, but may affect the top of the atmosphere (TOA) fluxes and heating rates near the tropopause. These high thin clouds are neglected in the present study. The effect of aerosols has also been neglected. Aerosol concentrations are typically small over the tropical oceans [*Smirnov et al.*, 2002]. Although aerosols will contribute to heating rates, the effect is expected to be small and the focus of this work is on the impact of clouds on radiative heating.

[14] Measurements of downwelling broadband longwave (LW; ~4 to 50 μm) and shortwave (SW; ~0.3 to 3 μm) radiation at the Manus and Nauru sites provide a means of testing the accuracy of radiative fluxes calculated using derived atmospheric properties. Radiative fluxes at the surface are measured by a suite of radiometers with 1-min sampling. The broadband LW radiation is measured by an Eppley precision infrared radiometer (PIR) pyrgeometer and the downwelling broadband SW radiation by an unshaded Eppley precision spectral pyranometer (PSP). Studies have shown that the component sum method for the measured broadband downwelling SW, which consists of combining the diffuse irradiance from the shaded Eppley PSP and the direct normal irradiance from the normal incidence pyrheliometer (NIP), reduces the errors associated with the cosine response of the unshaded PSP [*Michalsky et al.*, 1999]. However, at Nauru, the solar tracker was not operational from 6 August through 14 October, so the component sum method could not be applied. Comparisons of the measured SW at the surface from the component sum method and the unshaded PSP at Manus show an average difference of only 3.3 W/m^2 over the study period. Measurements of LW and SW fluxes at the TOA are obtained from products derived from a Geostationary Meteorological Satellite (GMS). The TOA radiative fluxes over the TWP region are available hourly at a resolution of 0.3 × 0.3° [*Nordeen et al.*, 2001]. These TOA fluxes are used to provide another radiative test of the derived radiative profiles.

3. Derived Cloud Properties

[15] The measured radar reflectivity and temperature profiles are used to retrieve profiles of cloud water content and particle size. Clouds with temperatures above 0°C are assumed to be liquid, and clouds below −16°C are assumed to be ice. Clouds at intermediate temperatures may be mixed phase. For liquid clouds, the profile of liquid water content (LWC) with height in the cloud is calculated from the regression equation of *Liao and Sassen* [1994], $LWC = \left(\frac{N_d Z}{3.6}\right)^{1/1.8}$, assuming a number concentration, N_d, of 100 cm^{-3}. Liquid clouds are

assumed to have a lognormal size distribution with a width of $\sigma = 0.35$ and a mode radius given by

$$r_m = \left(\frac{3LWC}{4\pi\rho_w N_d \exp\left(\frac{9}{2}\sigma^2\right)} \right)^{\frac{1}{3}},$$

where ρ_w is the density of water [*Frisch et al.*, 1995]. The value of N_d is based on the adiabatic model simulations of *Liao and Sassen* [1994], who found that $N_d = 100$ cm^{-3} gave the best agreement with empirically based reflectivity-liquid water relationships for cumulus and stratocumulus clouds, and is a reasonable value for marine stratocumulus clouds. In a review of in situ measurements of boundary layer clouds, *Miles et al.* [2000] found a mean value of $N_d = 74$ cm^{-3} with a standard deviation of 45 cm^{-3} for marine stratus and stratocumulus clouds. Similarly, the value of the lognormal width used is consistent with the values given by *Miles et al.* [2000]. The effective radius, r_e, used in subsequent radiative transfer calculations, is related to the mode radius through the expression: $r_e = r_m \exp\left(\frac{5}{2}\sigma^2\right)$ for a lognormal distribution. For ice clouds, the regression equation $IWC = (0.097)Z^{0.59}$ is used [*Liu and Illingworth*, 2000]. Ice effective radius, r_e, is parameterized as a function of temperature (°C), $r_e = (75.3 + 0.5895T)/2$ [*Ivanova et al.*, 2001].

[16] The retrieval of mixed phase cloud properties from remote sensing measurements is an active area of research. *Shupe et al.* [2004] used Doppler radar spectra to derive the microphysical properties of both the liquid and ice size distributions within a precipitating mixed phase altostratus cloud during the Cirrus Regional Study of Tropical Anvils and Cirrus Layers–Florida Area Cirrus Experiment (CRYSTAL-FACE). They found that the cloud ice contribution dominated the radar signal, accounting for 70 to 100% of the radar reflectivity through the depth of the cloud, and attributing the entire radar signal to ice in the retrieval overestimated the Ice Water Path (IWP) by only 7%. The LWC in the cloud was about 0.3 gm^{-3}, over a factor of 10 larger than the IWC throughout the cloud.

[17] Although ice may dominate the radar signal in mixed phase clouds, the liquid tends to dominate the radiative transfer because of the larger mass content and smaller particle sizes. There is little in situ information on mixed phase clouds in the tropics to verify or constrain remote sensing retrievals. In one of the most comprehensive studies of mixed phase clouds to date, *Korolev et al.* [2003] analyzed in situ aircraft observations of mixed phase clouds associated with midlatitude and Arctic frontal systems. They frequently found small amounts of liquid water present in clouds at temperatures down to −35°C and they found that 20 to 40% of clouds with temperatures between 0 and −15°C contained no measurable liquid. *Stith et al.* [2004] analyzed in situ measurements of tropical updrafts over the Amazon and Kwajalein. They found that most updrafts glaciated rapidly at temperatures between −5 and −17°C and liquid at temperatures less than about −17°C occurred only in brief segments of the flights. Similarly, *Heymsfield et al.* [2005] analyzed a convective case at temperatures below −30°C during CRYSTAL-FACE, and found liquid water only near the core updraft regions. Therefore we find it unlikely that there is significant LWC in most tropical clouds at temperatures less than about −16°C.

[18] *Korolev et al.* [2003] define a parameter u_3 = IWC/(IWC + LWC) and examine the cumulative probability of this parameter in various temperature regions. They consider any measurement with $u_3 > 0.9$ to be all ice because of measurement limitations. On the basis of the cumulative frequency distributions from *Korolev et al.* [2003], we create a simple scheme for deciding whether a particular cloud with temperature between 0°C and −16°C contains liquid. For each temperature, we take the cumulative probability of measurements having $u_3 <= 0.9$ to be the probability that a cloud layer contains some liquid. For each radar time step, we generate a random number uniformly distributed between 0 and 1. For each potentially mixed phase cloud layer, if the value of the random number is less than the cumulative probability of $u_3 <= 0.9$ at the temperature of the layer, then the layer is considered to contain some liquid; otherwise the layer is assumed to be glaciated. Thus the probability that a potentially mixed phase cloud layer contains liquid water ranges from 64% at −16°C to 100% at 0°C. We then determine the fraction of radar reflectivity associated with ice as a linear function of temperature, ranging from 100% at T = −16°C to 0% at T = 0°C. Once the reflectivity is divided into a liquid and ice component, the mass and effective radius of each component are calculated from the regression equations given above.

[19] After the distribution of LWC in the column has been determined, we scale the total LWP by the value retrieved from a dual-channel MWR using a statistical retrieval [*Westwater*, 1993]. Because the sensitivity of the MWR is 10 to 20 g/m^2 and nonzero amounts of LWP are often retrieved during clear sky because of differences between the actual water vapor and temperature profiles and the climatological values used in the retrieval, we scale the radar derived LWP only for columns where the derived LWP is greater than the MWR LWP.

4. Radiative Transfer Calculations

4.1. Model Description and Uncertainties

[20] The measured and derived atmospheric state parameters obtained from ARM measurements provide the inputs necessary to calculate radiative flux profiles. SW and LW broadband fluxes and radiative heating profiles are calculated using a delta-four-stream correlated k-distribution radiative transfer model [*Fu and Liou*, 1992]. We use an updated version of the model [*Rose and Charlock*, 2002] in which gas absorption coefficients were updated on the basis of the HITRAN 2000 database [*Rothman et al.*, 2003]. CFCs and CO_2 were added in the window region [*Kratz and Rose*, 1999] and the Clough-Kneizys-Davies (CKD) version 2.4 water vapor continuum absorption model [*Tobin et al.*, 1999] is used in the whole thermal spectrum (0–2850 cm^{-1}). The single-scattering properties of nonspherical ice particles are parameterized following *Fu* [1996] and *Fu et al.* [1998] while the single-scattering properties of water clouds are based on Mie calculations [*Fu et al.*, 1995].

[21] To reduce the time required for the radiative transfer calculations without introducing spurious artifacts caused by

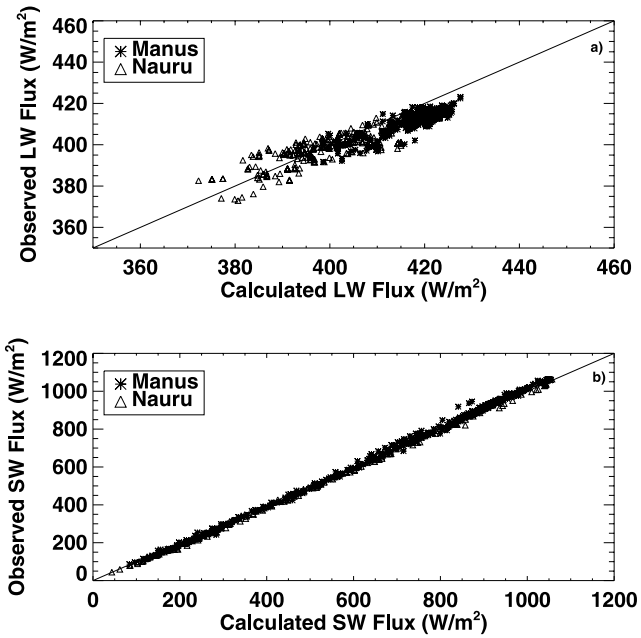

Figure 2. Clear-sky surface flux comparisons. The observed surface downwelling (a) longwave and (b) shortwave fluxes are plotted against the fluxes calculated using ARM observations for the atmospheric column properties. The one-to-one line (solid line) is plotted for reference.

averaging the cloud properties, we sampled the cloud property profiles every 5 min, resulting in over 26,000 profiles at Manus and 71,000 profiles at Nauru. The model was run with a vertical resolution of 45 m. The inputs to the radiative transfer algorithm are the retrieved vertical profile of cloud properties, temperature, humidity, and ozone. A Lambertian surface albedo of 0.05, which is representative of oceanic sites, is used for shortwave radiation calculations. To study the effect of clouds on the heating rate profiles and broadband fluxes, clear-sky profiles are calculated using the same atmospheric state profiles without including clouds.

[22] These calculations produce estimates of the heating rate profile that are compatible with the observed scale of the clouds in the column. Thin layers of clouds are often found in this region away from the central cores of convective elements. Their composite impact on the heating rate profile determines the vertical structure in these regions. Uncertainties in the cloud microphysics may impact the magnitudes of the heating in specific cloud layers, but it is expected that this uncertainty is small compared with the magnitude of the cloud heating.

[23] Uncertainties in retrieved cloud microphysical properties arise from approximations required because millimeter radar measurements are sensitive to the 6th moment of the droplet size distribution, while radiation is primarily sensitive to the 2nd moment of the size distribution. Uncertainties in retrievals of IWC are likely to have an error of about +100% and −50% [*Liu and Illingworth*, 2000]. Assuming random error, averaging over a long time series of measurements should reduce the impact of this uncertainty. However, an additional uncertainty in the IWC estimates arises because most in situ data used to develop radar retrievals were collected in midlatitude clouds. These measurements may not be truly representative of tropical clouds. Fresh anvil outflow from convection is likely to contain large aggregate particles that are not characteristic of midlatitude frontal clouds [*Heymsfield et al.*, 2005]. As these large particles precipitate from the anvil, the remnant particles and newly generated particles may more closely represent the midlatitude observations. Uncertainties for liquid cloud retrievals are likely reduced by the added measurement constraint imposed by MWR scaling. The estimated uncertainty in the MWR-derived LWP is the larger of 10% or 20 g m^{-2} [*Dong and Mace*, 2003].

[24] Additional uncertainties in the heating rate calculations include the neglect of high, thin cirrus, the specification of the vertical temperature and humidity profiles based on the 12-hourly radiosondes, the specification of surface albedo, neglect of aerosol, and treatment of gas absorption and cloud scattering in the radiative transfer model itself. Any individual heating rate profile is likely to have large uncertainties, but the impact of the uncertainties on the heating rates presented in this study is reduced because of averaging the data over a long time. In the next section, calculated fluxes are compared with measured fluxes. Sensitivities of heating rates to the uncertainty in the cloud properties and water vapor specification are examined in section 6.

4.2. Radiative Closure Tests

[25] While it is not currently possible to compare profiles of radiative fluxes to measurements at the ARM sites, there are radiative flux measurements available at the surface and the TOA. We have used surface flux measurements from the ARM TWP sites and TOA flux measurements derived from the GMS-5 satellite to provide a check on the flux calculations at the column boundaries. In the following comparisons, all differences are given in terms of calculated fluxes minus observed fluxes. Fluxes are separately compared for clear and all-sky conditions. The calculated and observed surface fluxes for daytime clear-sky periods are identified using the method of *Long and Ackerman* [2000] and compared. Only 146 min at Nauru and 404 min at Manus were classified as clear sky and corresponded to a time for which we had calculated heating rates. The calculated clear-sky downwelling fluxes at the surface are in good agreement with the observations at both sites, with average differences of less than 2% in the LW and less than 5% in the SW (Figure 2). This agreement is the same order of magnitude found in other clear-sky studies [e.g., *Kato et al.*, 1997].

[26] Observed and calculated fluxes are averaged over 20 min in all-sky conditions to reduce the discrepancy in the sampling from the narrow field-of-view instruments used to derive the cloud properties (MMCR and MWR) and the hemispheric field-of-view radiometers. Comparisons are made only for 20-min periods when the observed and calculated fluxes are available for at least 90% of the time. To compare the point calculations at the ARM sites to the satellite measurements, the ARM fluxes are averaged for 20 min with the averaging intervals centered on each satellite measurement time. Because the SW fluxes depend strongly on the solar zenith angle and because the sampling periods of the satellite and ground-based measurements are so different, the TOA broadband SW albedo is also used for comparison.

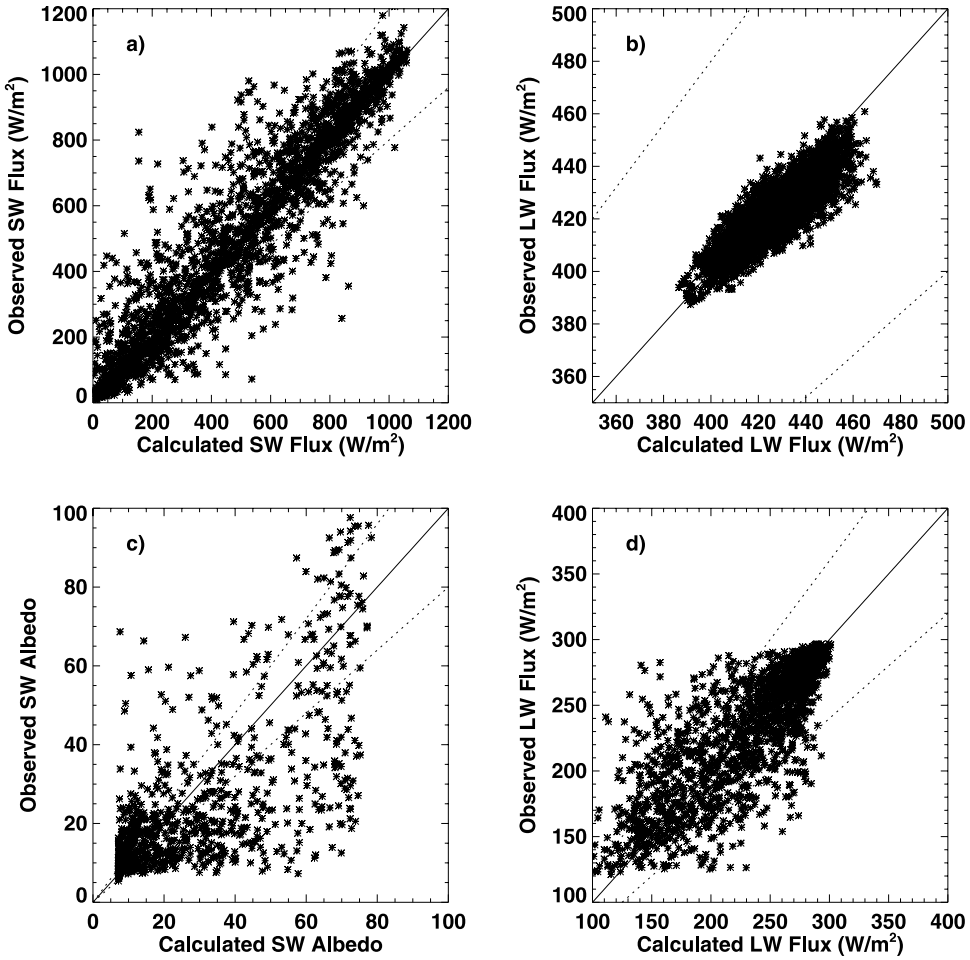

Figure 3. Comparisons of 20-min averaged calculated and observed fluxes under nonprecipitating conditions at Manus. (a) Downwelling SW flux at surface, (b) downwelling LW flux at surface, (c) SW albedo at TOA, and (d) upwelling LW flux at TOA. The one-to-one line (solid) and lines representing errors of ± 20% (dotted) are plotted for reference.

[27] The values of the mean observed flux, the mean difference between the calculated and observed flux, and the root-mean-square (RMS) difference are given in Table 1 for both Manus and Nauru. Comparisons of the calculated and observed fluxes at Manus are shown in Figure 3. Comparisons at Nauru (not shown) are similar.

[28] There is considerable scatter, but relatively low bias in the downwelling SW flux comparisons (Figure 3a). At both sites, the calculations tend to underestimate the amount of downwelling SW flux at the surface. At Nauru the bias is -23.1 W/m^2 (4% of the average downwelling flux) and at Manus the bias is -27.0 W/m^2 (5% of the average flux). The downwelling LW flux at the surface has a much smaller range because of the large amounts of water vapor in the tropical atmosphere. The calculations tend to slightly overestimate the amount of downwelling LW relative to the observations (Figure 3b) with a mean bias of 1.5 W/m^2 (0.4% of average measured flux) at Nauru and 4.9 W/m^2 (1.2%) at Manus.

[29] Good agreement exists between the observed and calculated outgoing longwave radiation (OLR) at the TOA although there tends to be scatter at intermediate values of OLR (Figure 3d). This scatter is not surprising because of the difference in spatial sampling of the GMS and surface observations. Manus has a lower average value of OLR (241.6 W/m^2) than Nauru (274.7 W/m^2), which is indicative of the more active convection and higher water vapor amounts over Manus.

Table 1. Comparison of Observed and Calculated Fluxes at Manus and Nauru[a]

	LW TOA, W/m^2	LW Surface, W/m^2	SW Albedo	SW TOA, W/m^2	SW Surface, W/m^2
		Manus			
Mean observed value	241.6	420.4	23.9	221.4	522.6
Mean difference	−0.7	4.9	3.8	34.5	−27.0
RMS difference	27.5	6.7	15.7	158.0	119.2
		Nauru			
Mean observed value	274.7	408.7	15.1	123.6	582.6
Mean difference	0.3	1.5	5.4	56.3	−23.1
RMS difference	20.0	9.1	11.6	119.4	104.7

[a]Differences between calculated and observed fluxes at Manus (top rows) and Nauru (bottom rows) for periods in which both valid GMS and surface observations exist. Calculated and surface fluxes are 20-min averages centered on the GMS observation time. Shortwave fluxes are averaged only over daytime observations. Flux differences are expressed as model minus observed flux.

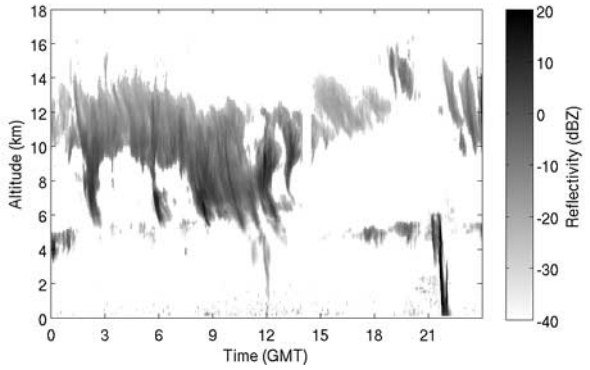

Figure 4. Radar reflectivity for Manus, 13 March 2000. A variety of cloud types are evident. Cirrus are present through much of the day and there are boundary layer clouds present for a short period between 0900 and 1300 UT. There is a thin cloud layer at 5 km present for much of the day. This melting level feature is a robust feature of long-term statistics. At two times, 1200 UT and 2200 UT, a vertical shaft extends to the ground. These shafts correspond to light drizzle events. A short period of missing radar data occurs near 1400 UT.

[30] The SW albedo comparisons show much larger disagreement between the calculations and the satellite observations (Figure 3c). At Nauru, the calculations overestimate the albedo at the TOA compared to the satellite observations for most periods. At Manus, the calculations and observations tend to agree for the lowest and highest values of reflected SW but disagree for midrange values. During suppressed conditions at Nauru (which were prevalent throughout 1999), the amount of low-level cloud is not representative of the larger area because of the effect of the island-influenced clouds, which can bias the cloud amount relative to the larger area seen by the satellite [*McFarlane et al.*, 2005]. Additionally, these shallow boundary layer cumulus clouds are often smaller than or comparable to the satellite resolution. Thus it is not surprising that the calculated TOA albedo, based on the radar observations, is higher than the satellite albedo. These clouds do not have a large impact on the OLR because of their low height. Further examination of the comparisons (not shown) suggests that the satellite TOA albedo exhibits a diurnal cycle related to the dependence of ocean albedo on solar zenith angle. This diurnal cycle is not seen in the calculations since a Lambertian surface albedo was used.

[31] The results of the flux comparisons indicate that the derived cloud property profiles are consistent with the surface radiation budget and are in reasonable agreement with the TOA radiation budget given the large differences in temporal and spatial sampling. This agreement inspires a reasonable level of confidence in the flux and heating rate profile calculations described in section 5.

5. Cloud and Radiative Heating Structures

[32] The technique outlined in the previous sections provides the means of calculating vertical distributions of cloud properties, radiative fluxes, and radiative heating rates. This procedure has been applied to measurements at Manus and Nauru. In the following sections, we examine characteristic features of the cloud and radiative heating profiles.

5.1. Cloud Field Characteristics

[33] An example plot of radar reflectivity illustrates many of the cloud types found in the tropics: shallow cumulus, altocumulus, altostratus, and cirrus (Figure 4). The detection statistics of these features are quantified using frequency distributions (Figure 5), similar to the contoured frequency by altitude diagrams (CFADs) developed by *Yuter and Houze* [1995] for C-band (5-cm wavelength) radar. The probability of observing a radar reflectivity value (Z) within a reflectivity range at a given altitude is shown in Figure 5a for the Manus period. At each height, the frequency of observing a given range of reflectivity values is illustrated by the color bar. Values of $Z < -60$ dBZ are assumed to be clear sky and are not shown, but they are included in the calculation of the frequency distributions. Below 5 km, there is a region of high reflectivity (> 0 dBZ) that is associated with precipitation. Although the MMCR can see through drizzling clouds, it saturates in heavy precipitation. The nonlinear increase indicated along the maximum reflectivity edge of the frequency distribution below 5 km is due to range correction of the saturation value of the receiver.

[34] *Johnson et al.* [1999] studied the distribution of radar echo-tops during TOGA-COARE and GATE using a

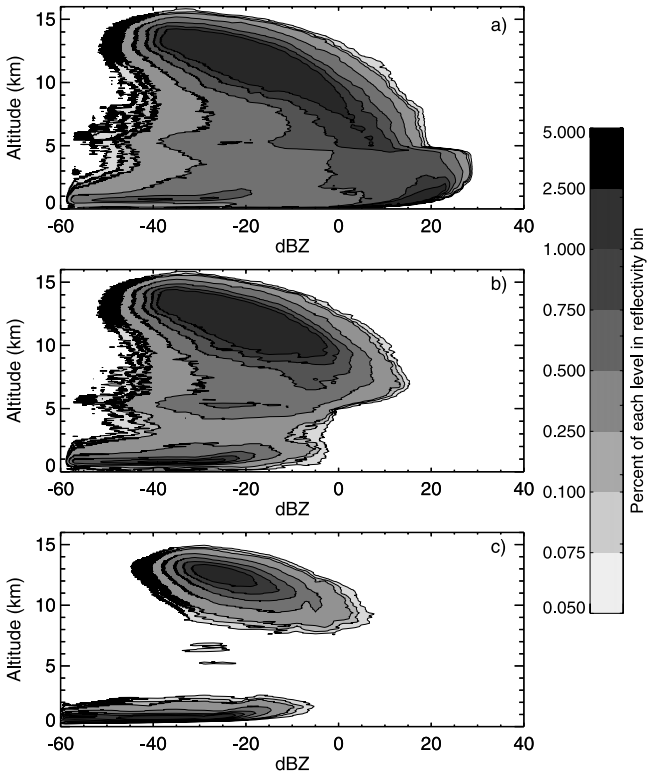

Figure 5. Reflectivity frequency distributions for (a) Manus, (b) Manus after precipitating columns have been removed, and (c) Nauru. Frequency is normalized by level. Clear sky (reflectivity values < -60 dBZ) is included in the normalization but not shown in the plot so that the frequency of clouds at each altitude can be seen.

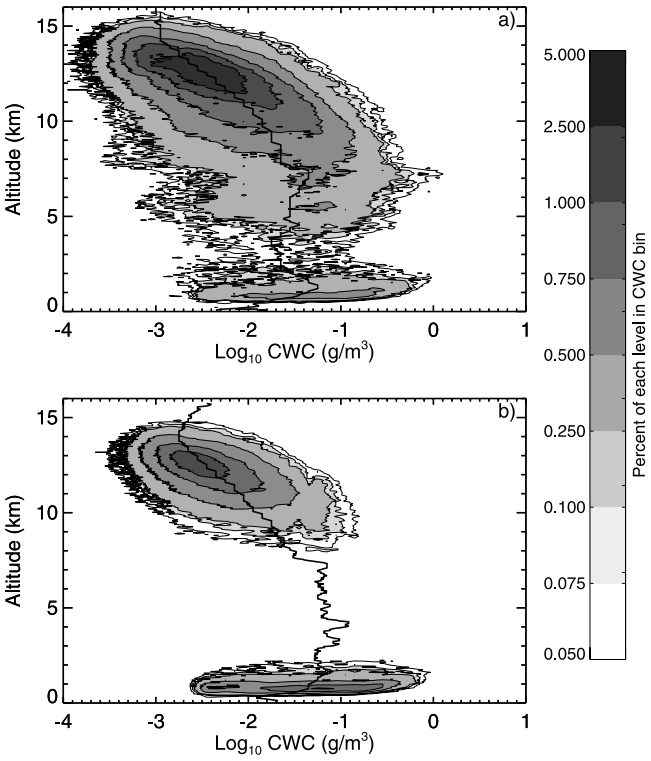

Figure 6. Condensed water content (CWC; liquid water content + ice water content) frequency distributions for nonprecipitating columns for (a) Manus and (b) Nauru. Frequency is normalized by level. The solid line in each panel represents the median CWC as a function of altitude.

C-band Doppler radar, which is sensitive to precipitation-sized particles, not cloud particles. They also found that the peaks in the distribution of echo-tops were located in three layers: near 2 km, near 5 km (0 C) and near 15 to 16 km. Examining the Manus MMCR observations, with the precipitation removed (Figure 5b), also reveals three distinct features in the vertical cloud profile. These features correspond roughly to moist layers (local maxima) in the mean relative humidity profile observed at Manus (Figure 1).

[35] In the lowest several kilometers, low reflectivity values (less than −10 dBZ) are indicative of liquid boundary layer clouds. This layer is also evident in a CFAD plot of the cloud condensed water content (CWC = LWC + IWC; Figure 6). The water content and radar reflectivity of these clouds increases with altitude. A peak in the relative humidity is found near 500 m at the base of this cloud layer (Figure 1). At the base of this layer, the median CWC is approximately 0.01 g/m^3 at both Manus and Nauru (Figure 6). At Manus, the median CWC rises to a peak of approximately 0.05 g/m^3 near an altitude of 1.3 km. At Nauru, the peak CWC is slightly larger (0.08 g/m^3) and occurs at a higher altitude (1.8 km). A second feature from 8 to 15 km corresponds to ice clouds consisting of cirrus and anvil outflow from deep convection. Clouds in this region exhibit a decrease in maximum reflectivity with height. This decrease likely reflects the settling of larger particles in ice cloud layers and the decrease in available water with altitude. The maximum frequency of occurrence of the ice cloud layer occurs between 12 and 13 km. At both Manus and Nauru, the median IWC is approximately 0.004 g/m^3 in this region of maximum cirrus occurrence (Figure 6). As noted previously, the radar is unable to detect optically thin cirrus clouds with small ice particles, so the actual peak cirrus occurrence likely occurs at a higher altitude [*Comstock et al.*, 2002].

[36] Above the boundary layer, between approximately 2 and 4 km, there is a minimum in cloud occurrence that is consistent with past studies [*Zuidema*, 1998]. However, at 5 km, a third cloud feature is observed that spans a wide range in reflectivity. This altitude corresponds to the melting level in the tropical Pacific and to another moist layer (Figure 1). The magnitude of the humidity peak at the melting level in Figure 1 is exaggerated because the relative humidity is calculated with respect to ice for temperatures below 0°C. Convective cloud tops are often seen in the radar data around 5 to 6 km. Previous analysis of tropical sounding data has identified a weak layer of enhanced stability near the melting level that may act as an impediment to deep convection [*Johnson et al.*, 1999]. Recent studies have indicated that the tendency of congestus clouds to have cloud tops near the melting level may be due to the entrainment of dry air commonly found between the boundary layer and the melting level [*Jensen and Del Genio*, 2006]. Detrainment from convective clouds in this stable layer may serve to moisten the layer in the vicinity of 5 to 6 km. Thin, single layer altocumulus clouds with low reflectivity are also frequently observed at this altitude, sometimes persisting for many hours. An example of such a layer can be seen between 1500 and 2000 UTC in Figure 4. Low radar reflectivity in association with many of these clouds suggests that they are primarily liquid. The vertical structure of the radar reflectivity distribution at Nauru (Figure 5c) is similar to the distribution at Manus, but there are significant differences in the frequency of the various cloud features. Boundary layer clouds are much more frequent in the Nauru observations, which is due primarily to the prevalence of island induced clouds at the Nauru site [*McFarlane et al.*, 2005]. Additionally, the Nauru period shows a considerable reduction of midlevel and precipitating clouds relative to the Manus data set, because of their differing locations. Nauru is located approximately 2000 km East of Manus, on the fringe of the West Pacific warm pool region. It experiences much greater interannual variability in convective activity and is much more sensitive to the phase of the El Nino/Southern Oscillation (ENSO) than Manus, which experiences convection throughout the year [*Mather*, 2005]. The shortwave cloud forcing can be viewed as a measure of convective activity and cloudiness at the two ARM sites (Figure 7). From 1999 through early 2001, the shortwave cloud forcing at Nauru was close to zero, indicating sparse cloud cover. During the same period, the Southern Oscillation Index (SOI) was relatively high. A high SOI corresponds to neutral or La Nina conditions and suppressed convection in the central Pacific. Suppressed conditions at Nauru were prevalent through the period of this study. The Nauru site experienced little organized convection during this early period of its operation.

5.2. Heating Rate Profiles

[37] Heating rate profiles provide a link between cloud properties, large-scale dynamics, and radiation. An example

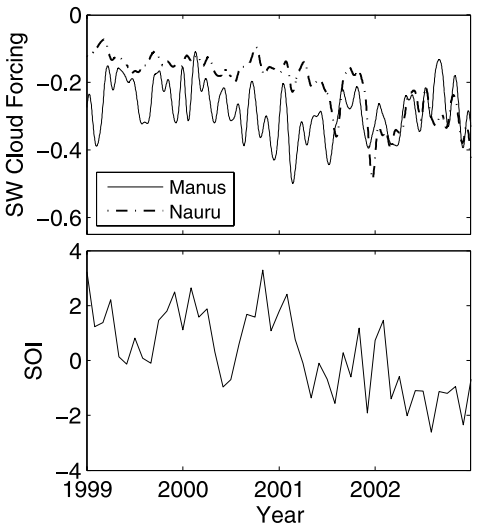

Figure 7. (top) A 4 year time series of surface SW cloud forcing measured at Manus (solid line) and Nauru (dash-dotted line). The shortwave cloud forcing is defined here as (SWobs-SWclr)/SWclr where SWobs is the measured surface downwelling shortwave flux while SWclr is the calculated clear sky surface downwelling shortwave flux. High values (close to zero) correspond to relatively clear sky conditions while large negative values correspond to higher cloud fractions. (bottom) Southern Oscillation Index from the National Weather Service Climate Prediction Center for the same 4 year period. Low values correspond to low-pressure perturbations at Tahiti relative to Darwin which in turn correspond to El Nino conditions.

of column radiative heating rates is given for 13 March 2000, at Manus (Figure 8). Comparing Figure 8 with the corresponding reflectivity profile (Figure 4) indicates heating in the lower portion of the cloud and cooling in the upper portion which may fuel internal circulations and mixing with surrounding clear air. Heating in the lower portion of the cloud is due to the temperature difference between cloud base and the surface below. The converse is true for cloud top. The instantaneous heating and cooling rates near the cloud boundaries can be quite large, often exceeding instantaneous rates of ±20 K/day. Clouds must be optically thick to produce cloud top cooling; optically thin clouds exhibit longwave heating at all levels [*Ackerman et al.*, 1988] and many of the cirrus observed in this study are too optically thin to produce cloud top cooling. Examples of such cirrus can be seen near 0100 UTC and 1500 UTC in Figure 8. Below the cirrus and midlevel layers, there are vertical streaks indicative of heating or reduced cooling (relative to the clear sky). This heating is generally in cloud-free regions and corresponds to absorption of infrared radiation emitted by the upper level clouds. The 13 March case also includes an altocumulus layer, perhaps generated by detrainment in the vicinity of the freezing level. A sharp heating rate gradient across this layer indicates that the layer is physically thin but optically thick caused by the presence of liquid water in the retrieved profile.

[38] This case study illustrates fairly typical vertical profiles of instantaneous radiative heating rates, which are expected to be important for cloud evolution. However, it is also of interest to consider the aggregate effect of radiative heating. To determine the impact of clouds on the temporally averaged radiative heating rate profiles, heating rate profiles were calculated using the same temperature/humidity profiles with and without clouds (Figure 9). The clear-sky profiles at the two sites (Figures 9a and 9b) are quite similar. The altitude of maximum cooling is slightly higher at Manus and cooling at the top of the boundary layer is not as strong; both are probably due to the larger water vapor amounts at Manus. The decrease in cooling rate above 10 km is caused by a combination of the drop-off in radiative cooling as the concentration of water decreases with temperature, and heating in the 9.6 μm O_3 bands and 15 μm CO_2 bands. This decrease in clear-sky radiative cooling near the tropopause may be important for stratosphere-troposphere exchange [*Gettelman et al.*, 2004]. The altitude at which net heating is zero is found near 15 km at both sites (slightly lower at Nauru), which is consistent with previous studies [*Gettelman et al.*, 2004].

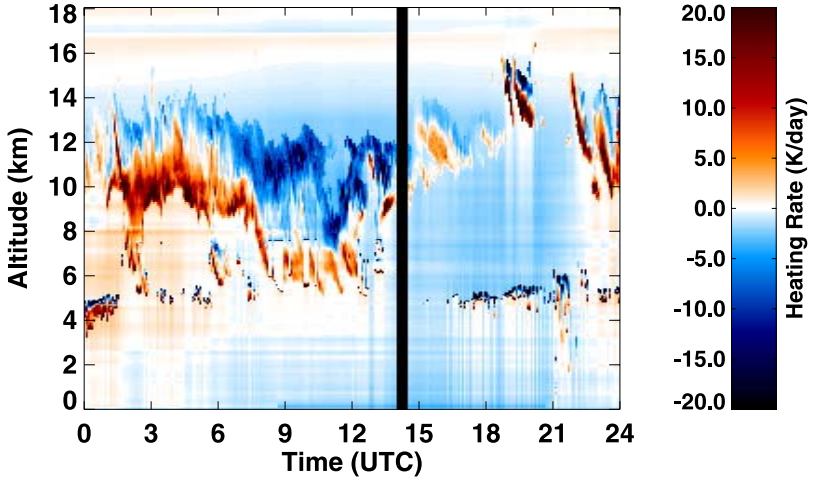

Figure 8. Calculated net heating rates for 13 March 2000 at Manus, corresponding to the radar reflectivity shown in Figure 4. Blues represent net cooling while reds represent net warming. Very dark colors represent heating/cooling greater than ±20 K/day.

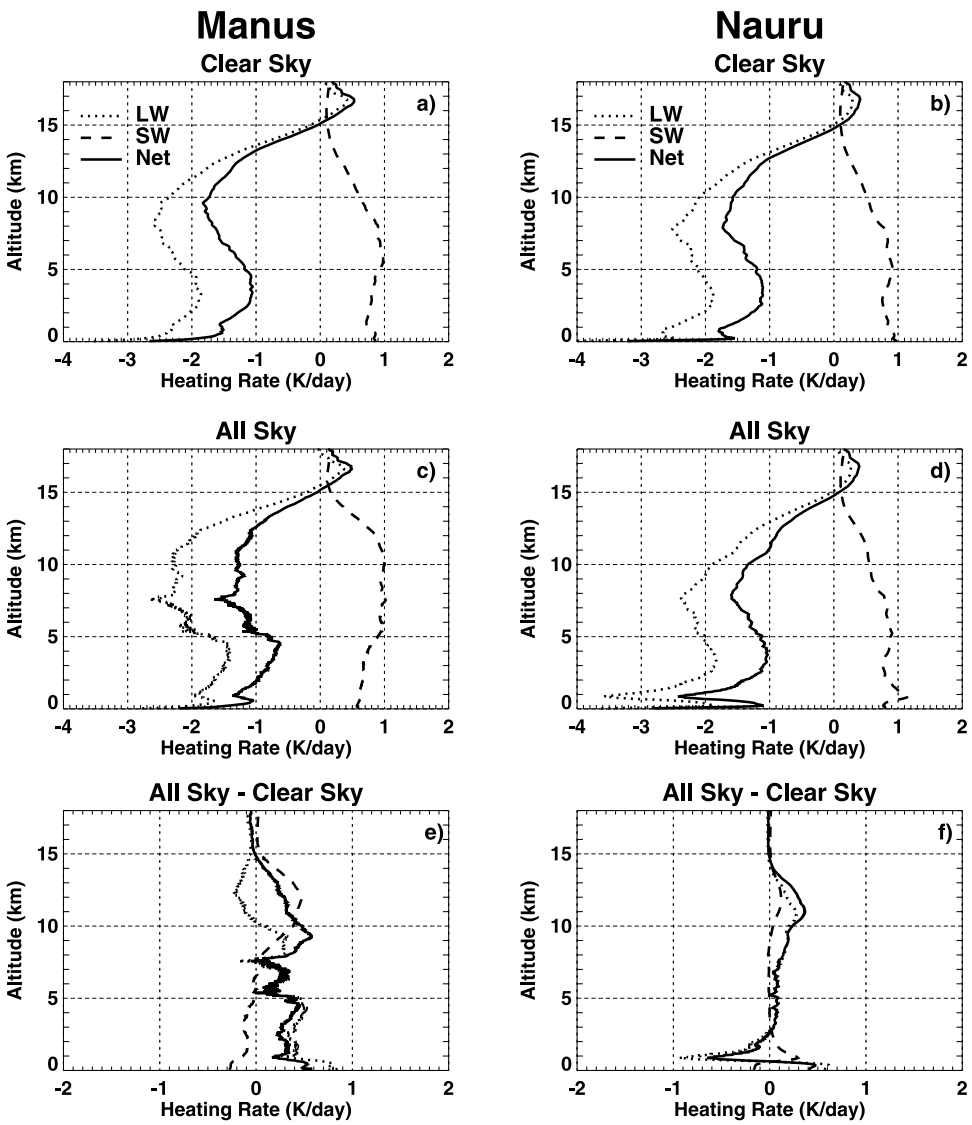

Figure 9. Average heating rates for Manus (left column) and Nauru (right column). Heating rate profiles are for (a and b) clear sky, (c and d) all sky, and (e and f) all sky minus clear sky.

[39] The impact of clouds on the heating rate profiles is most pronounced in the boundary layer and upper troposphere (Figures 9c–9f). At Nauru, there is a pronounced LW effect associated with boundary layer clouds: cooling within the cloud layer and heating below the layer (relative to clear sky). There is also significant SW heating within the cloud layer. The large magnitude of this feature reflects the high frequency of boundary layer clouds observed at Nauru and is less pronounced at Manus. Ice clouds also induce significant net heating above 8 km at both sites, which has a stabilizing impact on the troposphere. This heating is more pronounced at Manus because of a higher frequency of ice clouds. At both sites, peak cloud-induced radiative heating due to shortwave absorption is found near 12 km (Figures 9e and 9f), which corresponds to the peak in ice cloud occurrence (Figure 6). The peak in longwave radiative heating due to ice clouds is lower in altitude than the SW heating peak and is close to the base of the 8 to 15 km cirrus region. Unlike the 13 March case study (Figure 8) there is no evidence of cooling at cloud top in the long-term average. This indicates that the large instantaneous cooling rates are offset in the long-term averages by periods of heating (Figure 9).

[40] The height at which the average net radiative heating is zero is similar in the clear-sky and all-sky profiles, although previous sensitivity studies have indicated that the presence of clouds should raise the level of zero net heating due to longwave cooling above the clouds [*Gettelman et al.*, 2004]. These results show a slight lowering of the zero heating level due to clouds (Figures 9c and 9d). The inability of the radar to detect cirrus above 15 km may bias the heating rate profiles above this altitude; therefore conclusions should not be drawn from this study about the level of zero net heating in cloudy skies. Profiles from the two sites indicate little shortwave heating from beneath the ice cloud layer to the top of the boundary layer, though they differ slightly in their characterization of the profile. There is longwave heating (or reduced cooling relative to clear sky) between the boundary layer and the base of the cirrus layer as observed in the 13 March case. At Nauru, there are less midlevel and

high-level clouds than at Manus, so less induced heating occurs in the cloud-free regions.

[41] A sharp decrease in the cloud effect on the heating rate profiles at Manus is observed at 5 km (Figure 9e). This decrease is indicative of the cloud top cooling associated with these altocumulus and congestus clouds. A second cooling decrease near 7 km corresponds to a sharp gradient in the median condensed water content (Figures 9e and 6). This gradient, and the associated cooling feature, is likely a result of our treatment of the liquid/ice partitioning because this is the highest level at which clouds may contain liquid water in our scheme.

[42] The average net heating rate profiles can also be compared with previous studies including analyses of GATE [*Cox and Griffith*, 1979b] and TOGA-COARE [*Yang and Smith*, 2000; *Qian*, 2003]. Data from GATE collected in the tropical Atlantic, though relatively coarse in vertical resolution, indicate strong cooling of −2 K/day at the surface and a minimum in cooling of −0.5 K/day near 950 hPa [*Cox and Griffith*, 1979b, Figure 1]. In comparison, net heating rate profiles estimated from TOGA COARE data by *Qian* [2003, their Figure 1.15], which are of higher vertical resolution, show a cooling maximum of −1.5 K/day at the surface, a weaker minimum in net cooling of −1 K/day, and a secondary cooling maximum of −1.5 K/day at 950 hPa (approximately 600 m). The cooling minimum at the surface, boundary layer minimum, and secondary maximum are also found in the average heating rate profiles for both Manus and Nauru (Figures 9c and 9d), although the secondary maximum peak in the current study is somewhat higher (approximately 900 m) and larger in magnitude. This elevated boundary layer cooling peak has a magnitude of −1.6 K/day at Manus and −2.5 K/day at Nauru.

[43] Our results and the previous estimates for GATE and TOGA-COARE each show elevated cooling peaks for all-sky conditions. The results of *Cox and Griffith* [1979b] show a cooling maximum of approximately −1.5 K/day near 5 km with a gradual decrease in cooling with altitude. *Qian* [2003] reports dual cooling peaks at 6 and 12 km of −0.75 and −1 K/day respectively. The reduction in cooling between these levels is associated with strong (+1 K/day) radiative heating (primarily longwave) in cirrus. In the present study, there is a broad cooling peak between approximately 5 and 12 km with a peak near 8 km at both Manus and Nauru. Clear-sky cooling is offset by the longwave heating due to clouds, but the total cloud effect is only +0.5 K/day, less than reported by *Qian* [2003]. While the difference in these heating rate estimates is relatively small, the consequence of this difference, if applied over a large area in the tropics, could have a significant impact on the large-scale circulation.

[44] Large-scale circulation in the tropics is governed by the Hadley and Walker circulations. *Wang* [2002] has analyzed National Centers for Environmental Prediction (NCEP) – National Center for Atmospheric Research (NCAR) reanalysis data to construct climatologies of the Hadley and Walker circulations. At 11 km (250 hPa), which is near the center of the broad peak in radiative heating due to cirrus over Manus (Figure 9e), the mean vertical velocity associated with the Hadley cell in the vicinity of Manus is 0.5 cm/s. Following *Ackerman et al.* [1988] the impact of radiative heating in cirrus on vertical motion is estimated by applying a form of the thermodynamic energy equation:

$$\frac{R}{H}\frac{\partial T}{\partial t} + N^2 w = \frac{RQ}{H},$$

where R is the ideal gas constant, dT/dt is the local rate of temperature change, H is the scale height, N is the Brunt Vaisala frequency, w is the vertical velocity, and Q is the heating rate (expressed as temperature change per unit time). The Brunt Vaisala frequency is defined by:

$$N^2 = \frac{g}{\theta}\frac{\partial \theta}{\partial z},$$

where g is the acceleration due to gravity and θ is the potential temperature. Given the temperature profile in Figure 1, the Brunt Vaisala frequency at 11 km is approximately 7.5×10^{-3} s^{-1}. For the purpose of assessing the potential magnitude of the impact of the cloud radiative heating rate on vertical motion, it is assumed that the local rate of temperature change is zero so that the heating rate is balanced by adiabatic cooling associated with ascent. Over Manus, the heating at 11 km due to clouds is approximately 0.5 K/day. The ascent rate required to balance this cloud heating is approximately 0.4 cm/s, comparable to the magnitude of the Hadley cell. This suggests that the aggregate effect of radiative heating due to clouds may have an important impact on large-scale circulations.

[45] In the above calculations, the effects of latent heating are neglected for the purpose of assessing the potential impact of radiative processes. While latent heating cannot be ignored in a detailed calculation of the diabatic heating, the relative contribution of radiative heating is greater at higher altitudes, where the radiative heating peaks due to cirrus anvils, than at lower altitudes. Profiles of total heating from TOGA-COARE [e.g., *Lin et al.*, 2004; *Johnson and Ciesielski*, 2000] indicate that the peak in diabatic heating (including both latent and radiative heating) is found at approximately 7.5 km (400 hPa) and at 11 km (250 hPa), the relative impact of latent heating is greatly reduced.

5.3. Column Radiative Flux Divergence

[46] Net column heating rates may be computed by vertically integrating the individual heating rate profiles. This quantity is important because it represents the total amount of radiative energy deposited in the atmospheric column. The net column radiative heating rate must be balanced over time by latent heating and horizontal transport. The column heating rate is related to the tropospheric radiative convergence, which is defined as the net radiative flux at the tropopause minus the net radiative flux at the surface (net radiative components are defined as positive for downward fluxes). Tropospheric radiative convergence for GATE was found to have an average value of −120 W/m^2 with a range of −90 to −140 W/m^2 [*Cox and Griffith*, 1979b]. The average column heating rate associated with convergence is computed by applying the flux convergence to the total mass of the column. The heating rate is then given by:

$$\frac{dT}{dt} = \frac{g}{C_P}\frac{\Delta F}{\Delta P},$$

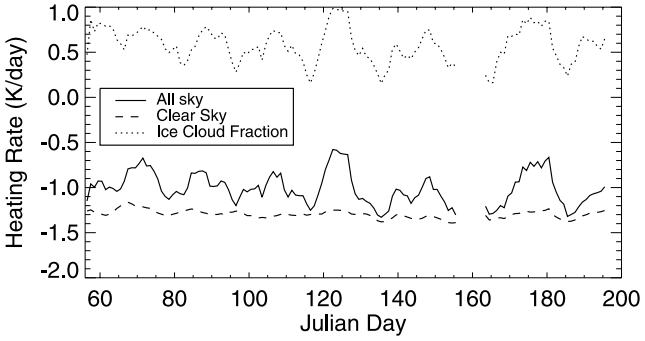

Figure 10. Five day averaged column heating rate and ice cloud fraction for Manus. Negative values indicate that the column is radiatively cooling.

where ΔF is the flux convergence across the layer and ΔP is the change in pressure across the layer.

[47] Cox and Griffith take the tropopause to be at 100 hPa and the surface pressure to be 1012 hPa. Applying the GATE radiative convergence to this layer yields a net column average heating rate of -1.1 K/day and a range of -0.8 to -1.3 K/day. *Qian* [2003] calculates longwave and shortwave column convergences and finds an average net column heating rate for TOGA COARE of -0.74 K/day with a range of -0.2 to -1.1 K/day.

[48] Net column convergence for the present study was computed excluding 24-hour periods with more than 50% of data missing. For periods with some missing data but less than 50% of data missing, the cloud frequency and LW fluxes are assumed to be representative of the entire 24-hour period. For the SW values, the ratio of the measured flux to the theoretical downwelling SW at the TOA is used to estimate the average SW flux at the surface. The average all-sky column (surface to 100 hPa) heating rate is -1.0 K/day and the average clear-sky heating rate is -1.3 K/day. The all-sky range of -0.5 K/day to -1.4 K/day (Figure 10) is similar to the results for GATE and TOGA COARE.

[49] *Ciesielski et al.* [2003] used a different technique to calculate the radiative flux convergence for TOGA COARE. The Ciesielski study calculated radiative heating rates as residuals of an energy budget analysis of radiosonde data following the work of *Yanai et al.* [1973]. This analysis of the TOGA COARE Intensive Flux Array data yields an average column heating rate of -0.55 K/day and a range of $+0.5$ K/day to -1.5 K/day. These positive excursions of the radiative column heating are not consistent with our results or other studies based on surface and TOA radiative fluxes. *Trenberth et al.* [2002] note that accounting for all energy terms in this sort of dynamically based energy budget is difficult, which is a conclusion supported by the present calculations. Although the present estimates differ with the *Ciesielski et al.* [2003] study in terms of the range in values, the correlation of the column heating to cloudiness is similar. Reduced column cooling is associated with high values of ice cloud fractions (Figure 10) as expected. The average heating rates in Figure 9 indicate that ice clouds have a warming effect in the shortwave in the cloud layer and a weak cooling effect below, while in the infrared they exhibit a warming effect throughout the column.

5.4. Diurnal Cycle

[50] The diurnal cycle of the heating rate profiles is calculated, beginning with clear sky. In these composites, vertical profiles for a given time of day at Manus are averaged temporally across 1-hour intervals (Figure 11). Not surprisingly, there is a strong diurnal cycle in the shortwave radiative heating. The peak magnitude, near local solar noon, is approximately 3 K/day and maximum heating rates are found near the surface and in the middle troposphere between approximately 5 and 8 km. This vertical structure is also evident in the long-term average plots (Figure 9). There is little evidence of a diurnal cycle in the clear-sky longwave radiative heating. Any diurnal structure in the clear-sky longwave cycle would have to be treated with caution because of the inadequate temporal resolution of the temperature and humidity observations. The clear-sky net heating rate composites reveal an interesting heating rate distribution with sharp temporal and vertical gradients. Although the maximum solar heating is found between 5 and 8 km, the daytime net heating

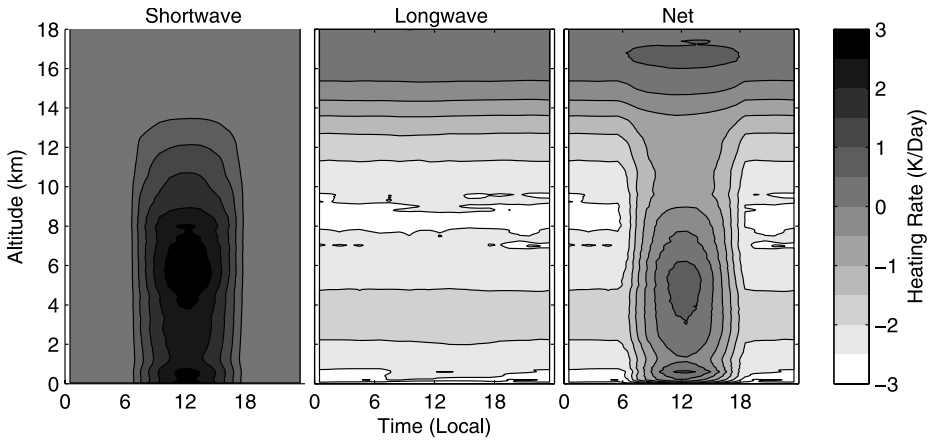

Figure 11. Diurnal composite of Manus (left) shortwave, (middle) longwave, and (right) net clear sky heating rates. Contour labels are heating rates with units of K/day. Positive values represent heating and negative values represent cooling. The data in this figure have been plotted with respect to local solar time to simplify interpretation of the diurnal cycle.

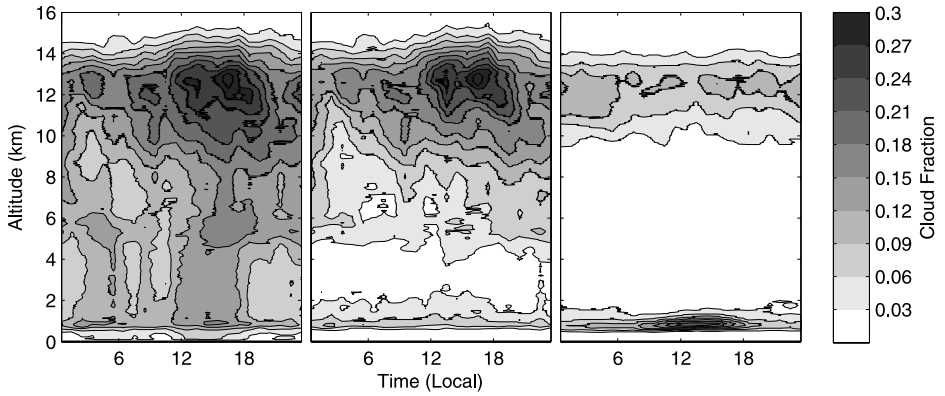

Figure 12. Diurnal composites of cloud occurrence for Manus and Nauru. (left) Composite for Manus with precipitation included. (middle) Composite for Manus with the precipitation removed and (right) composite for Nauru with the precipitation removed. These composites were produced by binning the cloud occurrence data by time of day and altitude and calculating the average heating rate for each time/altitude bin.

maximum is shifted to somewhat lower altitudes because solar heating in the higher altitude range is offset by strong longwave cooling.

[51] The diurnal cycle of hydrometeor (clouds and precipitation) and clouds-only (Figure 12) occurrence at Manus show that ice clouds and precipitation exhibit a strong diurnal cycle with peak occurrence of cirrus in the early afternoon (approximately 1500 local time). By comparing Figure 12 (left), which includes precipitation, and Figure 12 (middle), in which precipitation has been removed, it is seen that precipitation is most commonly observed in the afternoon and the early morning. The early morning precipitation maximum coincides with a minimum in cloudiness between approximately 7 and 10 km. The diurnal composite of radiative heating associated with clouds (Figure 13) shows a cooling maximum at the base of this dry layer. This combination of midlevel cooling and early morning convection is consistent with previous studies of the diurnal cycle in oceanic convection. These studies have proposed nocturnal midlevel infrared cooling and associated subsidence as a mechanism for forcing low-level convergence and early morning convection [*Foltz and Gray*, 1979; *Hall and Vonder Haar*, 1999].

[52] The occurrence of maximum convective activity near local noon matches satellite observations for the Manus region reported by *Neale and Slingo* [2003] in their Figure 7. The strong diurnal cycle at Manus is likely associated with its proximity to the large Maritime Continent islands of New Guinea, New Ireland, and New Britain [*Mather*, 2005]. Maximum rainfall over the large islands of the Maritime Continent (New Guinea, Borneo, Sumatra) occurs between 2000 and 0200 local time. Around these large islands there are broad (approximately 500 km across) bands where the time of maximum rainfall occurs between 0800 and 1400. Manus lies on the edge of one of these bands. This same study of the UK Met Office climate model [*Neale and Slingo*, 2003] indicates that the model does not accurately reproduce the diurnal cycle of convection within the maritime continent region. Therefore detailed observations of the diurnal cycle are an important area where ARM observations can be used to evaluate and improve climate model performance. Unlike Manus, Nauru is located far from any large landmass. The diurnal frequency of cloud occurrence (excluding precipitation cases) observed at Nauru for the 1999 study period is different than observed at Manus (Figure 12) for both cirrus and boundary layer clouds. There is a strong daytime maximum in the boundary layer cloud occurrence associated with fair weather cumulus generated by island heating while the cirrus actually exhibits a weak daytime minimum.

6. Sensitivity Tests

[53] Sensitivity tests were conducted to quantify potential uncertainty in the calculated heating rates and fluxes as a result of uncertainties in the specification of the microphysical and atmospheric state properties. Input properties were perturbed for the study period at Manus, and fluxes and heating rates were recomputed (Table 2). The changes in the average fluxes and heating rates were less than 15%; however, the instantaneous changes in individual cloudy

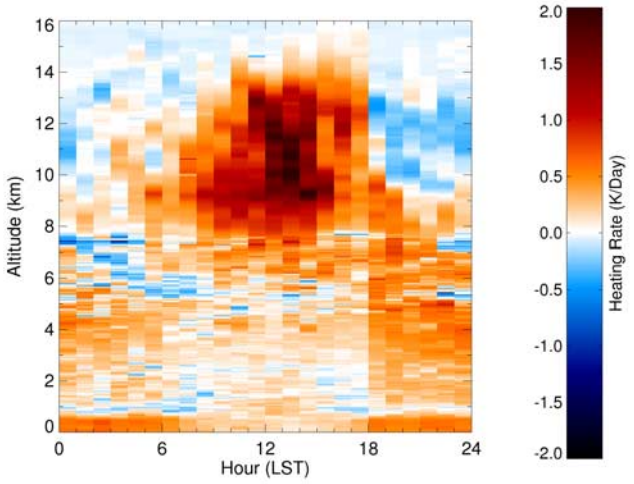

Figure 13. Diurnal composite all-sky minus clear sky heating rates for Manus.

Table 2. Sensitivity of Heating Rates to Particle Size, Water Content, and Water Vapor[a]

Parameter Adjusted	Amount of Change	Percent Change in LW TOA Flux	Percent Change in LW Surface Flux	Percent Change in SW TOA Albedo	Percent Change in SW Surface Flux
IWC	+100%/−50%	−3.3/2.9	0.1/−0.1	8.3/−6.7	−4.2/3.2
Ice particle size	+100%/−50%	3.0/−3.1	−0.1/0.1	−8.8/10.8	3.6/−4.5
LWC	+10%(or +20 g/m^2)/−10% (or −20 g/m^2)	−0.4/0.7	0.6/−0.7	13.0/−11.4	−7.4/5.6
Liquid particle size	+100%/−50%	0.1/0.0	−0.1/0.0	14.6/−12.2	5.1/−5.9
Water vapor	+10%/−10%	−0.8/0.8	1.2/−1.4	−0.3/0.3	−0.7/0.7

[a]For each sensitivity test, one cloud property parameter was systematically increased and decreased by the amounts given in the table, while the other cloud properties were held constant, and the heating rates were recalculated for the study period at Manus. For liquid clouds, the liquid water path was varied by the larger of 10% or 20 g/m^2.

profiles were occasionally much larger. The most sensitive component was the SW albedo, which changed by more than 8% for all changes in cloud properties and was equally sensitive to changes in liquid and ice clouds. The SW flux at the surface was also sensitive to changes in both liquid and ice clouds. The LW surface flux was the least sensitive to changes in the input properties, showing sensitivity primarily to a decrease in the LWC and to changes in water vapor. As expected, the LW flux at the TOA showed little sensitivity to changes in liquid cloud properties.

[54] Although the surface and TOA fluxes are relatively insensitive to these perturbations, the impact on heating rates is more significant. Sensitivities of the heating rates to changes in the cloud properties show that increasing IWC or decreasing ice particle size causes a small (less than 0.1 K/day) increase in the LW heating rate between 0 and 8 km, a larger (up to 0.25 K/day) increase in the LW heating rate between 5 and 12 km, and a small (0.05 K/day) decrease in the LW heating rate between 12 and 14 km (Figure 14). Comparing these profiles with the cloud profile frequency distribution (Figure 6) suggests that increasing the IWC results in an increase in LW cooling near cloud top, a strong increase in heating at cloud base, and a weaker increase in heating below the cloud that decreases with distance from cloud base. The SW heating rate shows a small (less than 0.05 K/day) decrease from 0 to 11 km, below the cirrus region, and an increase (up to 0.2 K/day) from 11 to 14 km, within the cirrus region. These somewhat compensating effects cause an increase (0.05 to 0.20 K/day) in the net heating rate from 5 to 8 km and a significant increase (0.20 to 0.35 K/day) from 9 to 14 km, with little net effect below 5 km. Decreasing IWC or increasing particle size shows a similar effect on the heating rates, but with the opposite sign. The effect of changing IWC or particle size by 100% leads to a 10 to 20% change in the average heating rate between 8 and 14 km.

[55] The effect of varying LWC by 10% or 20 g/m^2 has a much larger effect on the averaged heating rates than changing the liquid cloud particle size by 100% (Figure 15). Increasing LWC results in increased LW cooling within the mixed phase layer (up to 0.2 K/day) and within the boundary layer cloud region (up to 0.4 K/day) as well as increased warming (0.1 K/day) below the boundary layer cloud. There is small (less than 0.05 K/day) SW heating within the liquid cloud layers and SW cooling below the cloud layers. Decreasing the LWC results in changes of opposite sign in the heating rate profiles. Increasing (decreasing) effective radius by 100% leads to a small (less than 0.05 K/day) net warming (cooling) below the liquid cloud layer and little change elsewhere in the column, although changes in effective radius do have a large impact on SW albedo (Table 2). The liquid clouds, especially boundary layer clouds, occur in physically thin layers (generally less than 1 km deep) so the changes in the heating rates caused by changes in the liquid cloud properties are concentrated in narrow layers.

[56] Effects associated with the choice of retrieval equations for the ice properties were quantified by calculating the fluxes for the March 2000 data set using two different regression equations for r_e and IWC developed from in situ data from the Central Equatorial Pacific Experiment (CEPEX) by *McFarlane and Evans* [2004] and the CRYSTAL-FACE field project by J. Comstock (personal communication, 2005). Results from these sensitivity tests are given in Table 3. As in the previous sensitivity studies, the SW TOA albedo was the most variable component, with changes of up to 13.5% while the other flux components varied by less than 6%. Isolation of the events containing high clouds (Figure 16) shows that no choice of the regression equations gave better results for all components. The CEPEX results have a much smaller bias for the SW flux at the surface, but higher RMS difference (not shown) than the original results.

7. Summary and Conclusions

[57] Measurements at the ARM TWP sites, including profiles of reflectivity from MMCRs, provide the means to estimate cloud properties such as liquid and ice water content with high vertical and temporal resolution. Simple radar reflectivity/water content relationships have been applied to radar data from the ARM Manus and Nauru sites to obtain cloud properties with high temporal and vertical resolution for six months at Manus and for nine months at Nauru. Using the combination of these detailed cloud profiles with temperature and humidity profiles from radiosondes as input to a radiative transfer model, radiative fluxes and heating rates were calculated for the same analysis period.

[58] In this paper surface and TOA radiative flux measurements are used to test the accuracy of the calculated flux profiles. The results are generally encouraging with small biases in many of the comparisons. At the surface and TOA, average differences between observed and calculated fluxes are approximately 5% or less of the average measured flux. Calculated residuals suggest that the TOA shortwave component is the most problematic in terms of closure. The average differences between observed and calculated TOA albedo are 20 to 30% of the average albedo. This is likely caused, in part, by the strong spatial variability in albedo associated with convective towers. A better understanding of this component will be a focus of future work.

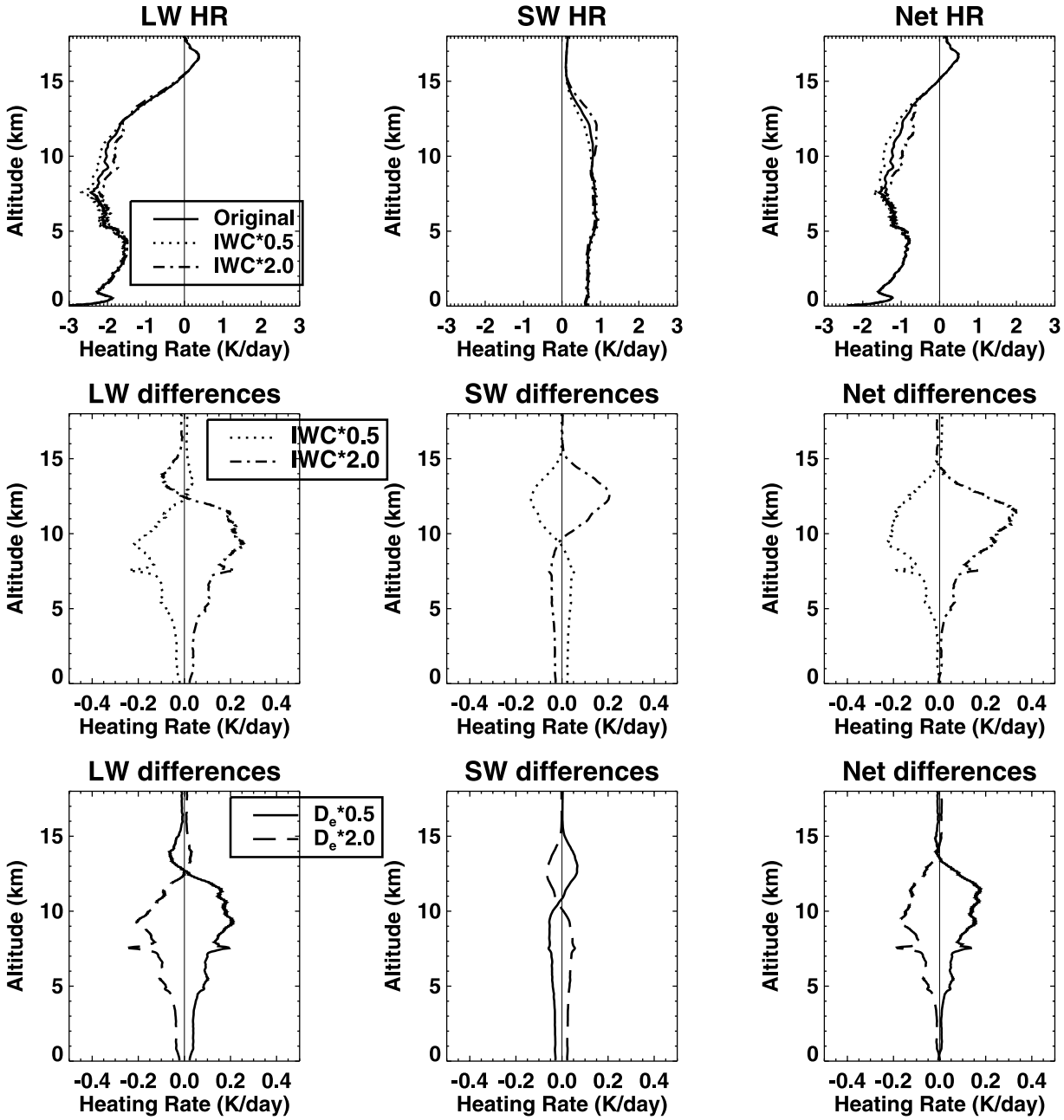

Figure 14. Sensitivity tests for ice water content (IWC) and effective diameter (De). Radiative calculations were reproduced for all cases with the IWC increased by a factor of 2 (*2) and decreased by a factor of 2 (*0.5) while all other parameters were held constant. (top) Resulting heating rate profiles for longwave (LW), shortwave (SW), and the net heating rate (LW + SW) and (middle) change in the heating rate profiles relative to the best estimate case given changes in the ice water content. (bottom) Change in the heating rate profiles given changes in the ice particle effective diameter.

[59] Analyses of the cloud property and radiation profiles reveal several interesting features in the vertical cloud distribution and in the resulting radiative heating rates. There is clear evidence of a trimodal cloud structure with peaks in the boundary layer (shallow convection), in the upper troposphere (outflow from deep convection), and near 5 km (detrainment at the freezing level). The midlevel feature near the freezing level is found only at Manus, which was more convectively active than Nauru during the study periods. The cirrus feature is similar in shape between the two sites (covering a similar range of altitudes and ice water content) but clouds occur much more frequently at Manus in the range of 8 to 15 km. In the upper troposphere, retrieved ice water content decreases with altitude, which is consistent with in situ observations of tropical cirrus. In the shallow convective clouds, the liquid water content increases with altitude.

[60] These cloud features have significant impacts on the radiative heating rate profiles over Manus and Nauru. Long-term averages of radiative heating rate profiles show

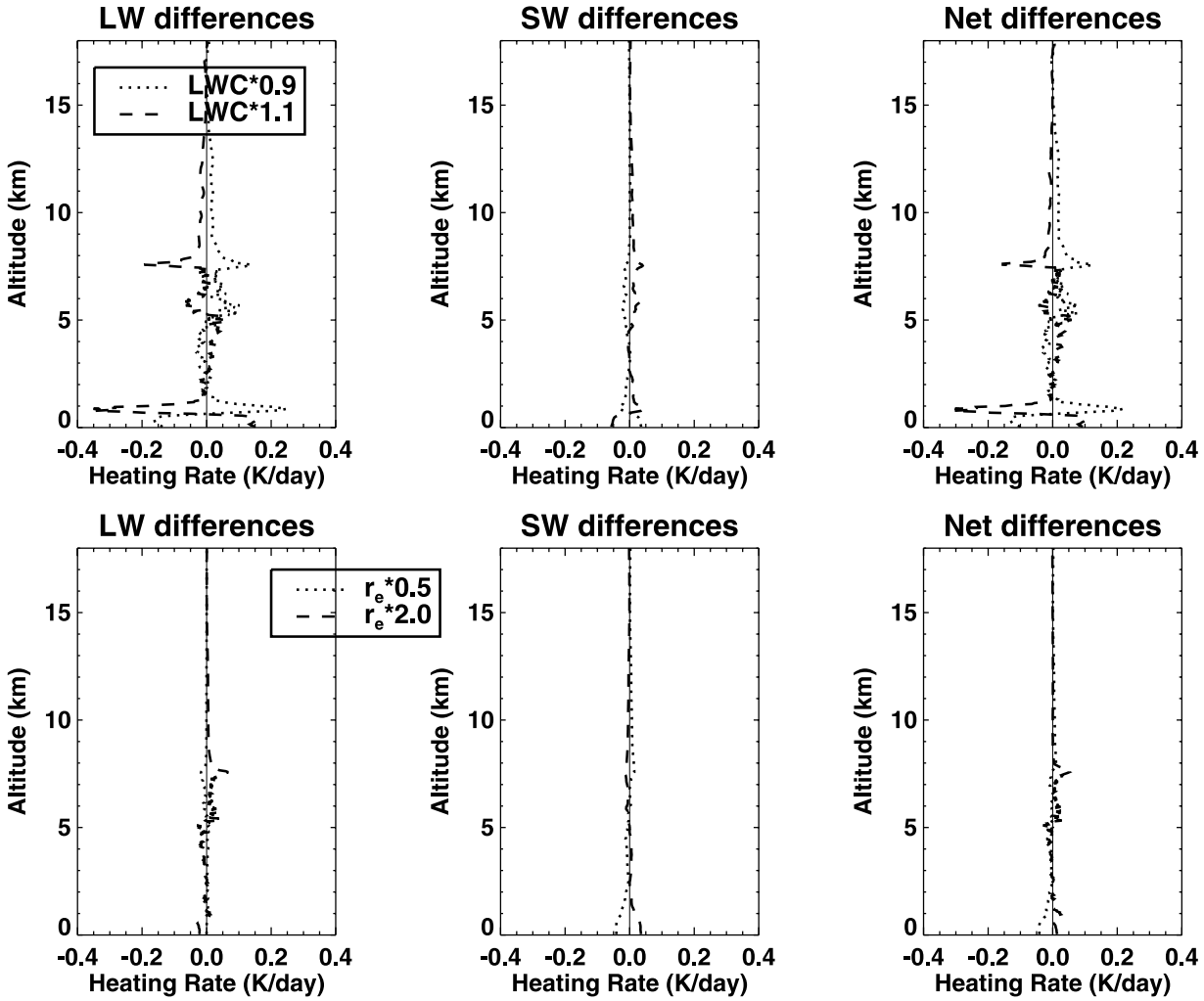

Figure 15. Sensitivity tests as described in Figure 14 but for ranges in liquid water content (LWC) and water droplet effective radius (r_e).

the largest radiative impacts are due to clouds in the boundary layer (heating below cloud level and cooling above) and between 8 and 14 km (heating). There are also differences between the heating rate profiles at Manus and Nauru. Cloud induced heating at cirrus levels is more pronounced at Manus than at Nauru. At midlevels, between 2 and 8 km, there is more heating and vertical structure at Manus than at Nauru. Nauru experiences stronger radiative effects associated with boundary layer clouds with very strong cooling at the top of the boundary layer and heating below cloud level.

[61] The sensitivity of heating rates to some of the assumptions used for calculating cloud properties has also been examined. These tests reveal the effects of the uncertainties in cloud properties on the heating rates and highlight characteristics of the interaction between clouds and radiation. Increasing the ice water content or decreasing ice particle size results in increased heating within the cloud layer but longwave and shortwave effects approximately cancel each other above and below the cloud layer. Thus sensitivity to these ice parameters is confined to a relatively narrow altitude band. Sensitivity to liquid water content is strongest in the boundary layer where increasing the liquid water content increases cooling at cloud top and heating in the boundary layer. Particle size has little impact on heating associated with these boundary layer clouds. The parameterizations for cloud ice, liquid water content, and particle size are relatively simple. However, the first-order

Table 3. Sensitivity of Radiative Fluxes to IWC Parameterization[a]

Regression Used	Percent Change in LW TOA Flux	Percent Change in LW Surface Flux	Percent Change in SW TOA Albedo	Percent Change in SW Surface Flux
CEPEX	1.7	−0.1	−8.0	3.9
CRYSTAL	4.3	−0.1	−13.5	5.8

[a]Changes in calculated fluxes due to using different regression equations to retrieve IWC and ice particle size for the month of March 2000 at Manus.

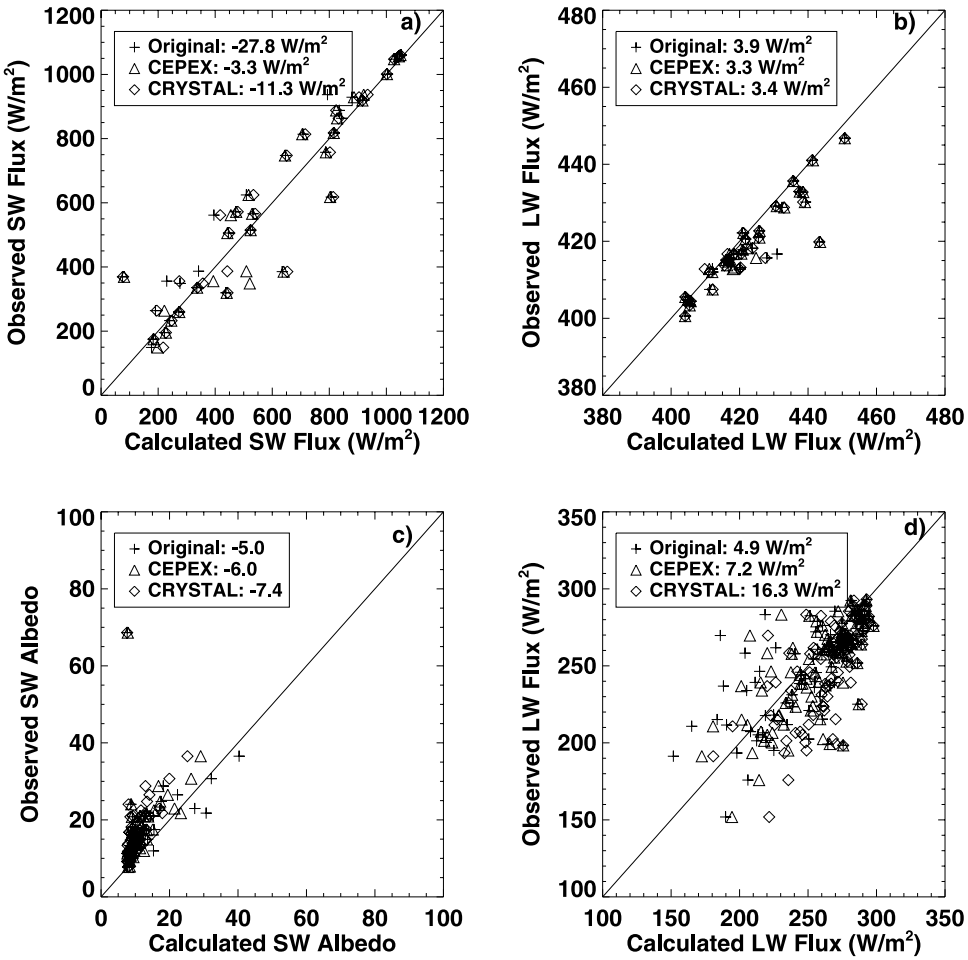

Figure 16. Comparisons of 20-min averaged calculated and observed fluxes for periods at Manus during March 2000 with only high clouds. (a) SW flux at surface, (b) LW flux at surface, (c) SW albedo at TOA, and (d) LW flux at TOA. Values given in the legend represent the average flux differences (calculated minus modeled) for the various regression methods used.

effect of clouds on the vertical heating profile is associated with their location. Although the magnitude of heating in these results may be refined when better parameterizations become available, the vertical structure should be quite good except for missing thin cirrus near the tropopause. These results will provide a baseline that can be used for development and evaluation of more sophisticated cloud property retrievals.

[62] This study focuses on examining the characteristics of long-term averages, which provides interesting insights to tropical clouds and radiation and allows these results to be compared to previous studies of tropical heating rates. The high temporal resolution of these data makes it possible to examine the interaction of tropical clouds and radiation in many other ways. One simple example of these applications is the illustration of cloud and heating rate diurnal composites. These results show a pronounced difference in the diurnal cycles at Manus and Nauru. Cirrus exhibit a strong diurnal cycle at Manus with corresponding effects on heating rates, while the diurnal cycle in cirrus at Nauru is much weaker.

[63] Radiative heating is expected to have a direct impact on driving atmospheric vertical motion. The high temporal resolution of these data will make it possible to study the instantaneous heating rates of cloud systems. These data can be used to examine the impact of cloud-radiation interactions on cloud evolution or to examine the relative impacts of radiative and latent heating on convective cloud systems. The potential impact of averaged radiative heating on large-scale motion has been examined briefly. This simple analysis suggests that radiative heating in cirrus may play a significant role in the strength of large-scale tropical circulation. In future work, the links between radiative heating and atmospheric motion on a range of timescales will be examined further.

[64] A key goal of the ARM Program is to apply its measurements for the improvement of climate models. One useful way to bridge the gap between ARM observations and climate models is to generate data products from the ARM observations that can readily be compared to climate model parameters. The cloud products and resulting radiative heating rate profiles described in this paper represent such a link between observations and simulations. These data sets, which describe the characteristics of the cloud and radiation fields over the ARM tropical sites, will provide a useful tool for examining the accuracy of these fields in

model simulations as well as for studying the atmospheric processes that produce these fields.

Appendix A: Interpolated Sounding Profiles

[65] Column water vapor amounts and temperature profiles in the near surface layer may change on timescales that cannot be resolved by the 12-hourly radiosonde launches. An iterative scaling approach is used to produce a thermodynamic time series that is consistent with the MWR and surface temperature measurements, preserves the vertical structure near the time of the radiosonde launches and is physically reasonable throughout the column.

[66] The column water vapor measured by the radiosonde is scaled to match the microwave radiometer column vapor at the corresponding time, which has been shown to be more accurate by providing sonde to sonde consistency [*Turner et al.*, 2003]. The microwave and surface temperature data sets are interpolated to a uniform 20-min time grid, and the radiosonde temperature and water vapor profiles are linearly interpolated to the same time grid. The interpolated temperature profile is constrained to a diurnal profile near the surface following the procedure of *Hollars* [2004]. In this procedure, the linearly interpolated radiosonde temperature is blended with the diurnal shape of the surface air temperature. The temperature at time, t, and height, z, is given by

$$T(t,z) = W(t)T_i(t,z) + (1 - W)R(z)T(ts,z),$$

where $T_i(t, z)$ is the linearly interpolated temperature at the given time and height and T(ts, z) is the temperature at the given height from the original radiosonde launched at time ts. W is a dimensionless number that captures the diurnal tendency of the surface temperature:

$$W(t) = T_{sfc}(t)/T_{sfc}(ts),$$

where T_{sfc} is the temperature measured by the surface air temperature sensor. R is a dimensionless number that reduces the impact of the surface temperature diurnal cycle as altitude increases:

$$R(z) = 1 + (z - z_{max})/z_{max} \qquad z < z_{max}$$

$$R(z) = 1 \qquad z >= z_{max}$$

[67] In this scheme, the influence of the observed surface air temperature controls the interpolated radiosonde temperature at the surface but its influence diminishes with height dropping to zero by z_{max}. In this study, z_{max} is taken to be 600 m.

[68] The interpolated water vapor profiles are scaled to match the MWR column value on the 20-min time grid using an iterative procedure. If the interpolated profiles are simply scaled to the MWR value, unrealistically high values of supersaturation with respect to water may result. To avoid this problem, when the radiosonde is dry relative to the MWR, the relative humidity is gradually increased by a uniform fraction of 100 − RH(z) where RH(z) is the relative humidity as a function of height. Thus, if RH = 100% at a given altitude, the RH is not increased. In this way, the general shape of the water vapor profile is preserved without unrealistic values of supersaturation.

[69] **Acknowledgments.** The Pacific Northwest National Laboratory is operated by Battelle for the U.S. Department of Energy (DOE). This research was supported by the DOE office of Biological and Environmental Research under contract DE-AC05-76RL01830 as part of the Atmospheric Radiation Measurement (ARM) program. Southern Oscillation Index data were obtained from the National Weather Service Climate Prediction Center, http://www.cpc.ncep.noaa.gov.

References

Ackerman, T. P., K.-N. Liou, F. P. J. Valero, and L. Pfister (1988), Heating rates in tropical anvils, *J. Atmos. Sci.*, *45*, 1606–1623.

Bergman, J. W., and H. H. Hendon (1998), Calculating monthly radiative fluxes and heating rates from monthly cloud observations, *J. Atmos. Sci.*, *55*, 3471–3491.

Ciesielski, P. E., R. H. Johnson, P. T. Haertel, and J. Wang (2003), Corrected TOGA COARE Sounding humidity data: Impact on diagnosed properties of convection and climate over the warm pool, *J. Clim.*, *16*, 2370–2384.

Clothiaux, E. E., et al. (1999), The Atmospheric Radiation Measurement program cloud radars: Operational modes, *J. Atmos. Oceanic Technol.*, *16*, 819–827.

Clothiaux, E. E., T. P. Ackerman, G. G. Mace, K. P. Moran, R. T. Marchand, M. A. Miller, and B. E. Martner (2000), Objective determination of cloud heights and radar reflectivities using a combination of active remote sensors at the ARM CART sites, *J. Appl. Meteorol.*, *39*, 645–665.

Comstock, J. M., T. P. Ackerman, and G. G. Mace (2002), Ground-based lidar and radar remote sensing of tropical cirrus clouds at Nauru Island: Cloud statistics and radiative impacts, *J. Geophys. Res.*, *107*(D23), 4714, doi:10.1029/2002JD002203.

Cox, S. K., and K. T. Griffith (1979a), Estimates of Radiative divergence during phase III of the GARP Atlantic Tropical Experiment: Part I. Methodology, *J. Atmos. Sci.*, *36*, 576–585.

Cox, S. K., and K. T. Griffith (1979b), Estimates of Radiative divergence during phase III of the GARP Atlantic Tropical Experiment: Part II. Analysis of phase III results, *J. Atmos. Sci.*, *36*, 586–601.

Dong, X., and G. G. Mace (2003), Profiles of low-level stratus cloud microphysics deduced from ground-based measurements, *J. Atmos. Oceanic Technol.*, *20*, 42–53.

Foltz, G. S., and W. M. Gray (1979), Diurnal variation in the troposphere's energy balance, *J. Atmos. Sci.*, *36*, 1450–1466.

Frisch, A. S., C. W. Fairall, and J. B. Snider (1995), Measurement of stratus cloud and drizzle parameters in ASTEX with a K_α-band Doppler radar and a microwave radiometer, *J. Atmos. Sci.*, *52*, 2788–2799.

Fu, Q. (1996), An accurate parameterization of the solar radiative properties of cirrus clouds for climate models, *J. Clim.*, *9*, 2058–2082.

Fu, Q., and K. N. Liou (1992), On the correlated k-distribution method for radiative transfer in nonhomogeneous atmospheres, *J. Atmos. Sci.*, *49*, 2139–2156.

Fu, Q., S. K. Krueger, and K. N. Liou (1995), Interactions between radiation and convection in simulated tropical cloud clusters, *J. Atmos. Sci.*, *52*, 1310–1328.

Fu, Q., P. Yang, and W. B. Sun (1998), An accurate parameterization of the infrared radiative properties of cirrus clouds for climate models, *J. Clim.*, *11*, 2223–2237.

Gettelman, A., P. M. de F. Forster, M. Fujiwara, Q. Fu, H. Vömel, L. K. Gohar, C. Johanson, and M. Ammerman (2004), Radiation balance of the tropical tropopause layer, *J. Geophys. Res.*, *109*, D07103, doi:10.1029/2003JD004190.

Grabowski, W. W., and M. W. Moncrieff (2002), Large-scale organization of tropical convection in two-dimensional explicit numerical simulations: Effects of interactive radiation, *Q. J. R. Meteorol. Soc.*, *128*, 2349–2375.

Gu, Y., and K. N. Liou (2000), Interactions of radiation, microphysics, and turbulence in the evolution of cirrus clouds, *J. Atmos. Sci.*, *57*, 2463–2479.

Hall, T. J., and T. H. Vonder Haar (1999), The diurnal cycle of west Pacific deep convection and its relation to the spatial and temporal variation of tropical MCSs, *J. Atmos. Sci.*, *56*, 3401–3415.

Heymsfield, A. J., L. M. Miloshevich, C. Schmitt, A. Bansemer, C. Twohy, M. R. Poellot, A. Fridlind, and H. Gerber (2005), Homogeneous ice nucleation in subtropical convection and its influence on cirrus anvil microphysics, *J. Atmos. Sci.*, *62*, 41–64.

Hollars, S. C. (2004), Radiative regulations on cloud behaviors in the Tropical Western Pacific, Master's thesis, Dep. of Atmos. Sci., Univ. of Wash., Seattle.

Houze, R. (1989), Observed structure of mesoscale convective systems and implications for large-scale heating, *Q. J. R. Meteorol. Soc.*, *115*, 425–461.

Ivanova, D. D., L. Mitchell, W. P. Arnott, and M. Poellot (2001), A GCM parameterization for bimodal size spectra and ice mass removal rates in mid-latitude cirrus clouds, *Atmos. Res.*, *59*, 89–113.

Jakob, C., and G. Tselioudis (2003), Objective Identification of cloud regimes in the Tropical Western Pacific, *Geophys. Res. Lett.*, *30*(21), 2082, doi:10.1029/2003GL018367.

Jensen, M. P., and A. D. Del Genio (2006), Factors limiting cloud-top height at the ARM Nauru Island climate research facility, *J. Clim.*, *19*, 2105–2117.

Jensen, M. P., T. P. Ackerman, and S. M. Sekelsky (2002), Radiative impacts of anvil cloud during the Maritime Continent Thunderstorm Experiment, *J. Appl. Meteorol.*, *41*, 473–487.

Johnson, R. H., and P. E. Ciesielski (2000), Rainfall and radiative heating rates from TOGA COARE Atmospheric Budgets, *J. Atmos. Sci.*, *57*, 1497–1514.

Johnson, R. H., T. M. Rickenback, S. A. Rutledge, P. E. Ciesielski, and W. H. Schubert (1999), Trimodal characteristics of tropical convection, *J. Clim.*, *12*, 2397–2418.

Kato, S., T. P. Ackerman, E. E. Clothiaux, J. H. Mather, G. G. Mace, M. L. Wesley, F. Murcray, and J. Michalsky (1997), Uncertainties in modeled and measured clear-sky surface shortwave irradiances, *J. Geophys. Res.*, *102*, 25,881–25,898.

Korolev, A. V., G. A. Isaac, S. G. Cober, J. W. Strapp, and J. Hallett (2003), Microphysical characterization of mixed-phase clouds, *Q. J. R. Meteorol. Soc.*, *129*, 39–65.

Kratz, D., and F. Rose (1999), Accounting for molecular absorption within the spectral range of the CERES window channel, *J. Quant. Spectrosc. Radiat. Transfer*, *48*, 83–95.

Larson, K., D. L. Hartmann, and S. A. Klein (1999), The role of clouds, water vapor, circulation, and boundary layer structure in the sensitivity of the tropical climate, *J. Clim.*, *12*, 2359–2374.

Liao, L., and K. Sassen (1994), Investigation of relationships between Ka-band radar reflectivity and ice and liquid water contents, *J. Atmos. Sci.*, *35*, 231–248.

Lin, J., B. Mapes, M. Zhang, and M. Newman (2004), Stratiform precipitation, vertical heating profiles, and the Madden-Julian Oscillation, *J. Atmos. Sci.*, *61*, 296–309.

Liu, C. L., and A. J. Illingworth (2000), Toward more accurate retrievals of ice water content from radar measurements of clouds, *J. Appl. Meteorol.*, *39*, 1130–1146.

Long, C. N., and T. P. Ackerman (2000), Identification of clear skies from broadband pyranometer measurements and calculation of downwelling shortwave cloud effects, *J. Geophys. Res.*, *105*, 15,609–15,626.

Mather, J. H. (2005), Seasonal variability in clouds and radiation at the Manus ARM site, *J. Clim.*, *18*, 2417–2428.

Mather, J. H., T. P. Ackerman, W. E. Clements, F. J. Barnes, M. D. Ivey, L. D. Hatfield, and R. M. Reynolds (1998), An atmospheric radiation and cloud station in the Tropical Western Pacific, *Bull. Am. Meteorol. Soc.*, *79*, 627–642.

McFarlane, S. A., and K. F. Evans (2004), Clouds and shortwave fluxes at Nauru. Part I: Retrieved cloud properties, *J. Atmos. Sci.*, *61*, 733–744.

McFarlane, S. A., C. N. Long, and D. M. Flynn (2005), Impact of island-induced clouds on surface measurements: Analysis of the ARM Nauru Island effect study data, *J. Appl. Meteorol.*, *44*, 1045–1065.

Michalsky, J., E. Dutton, D. Nelson, M. Rubses, T. Stoffel, M. Wesley, M. Splitt, and J. deLuisi (1999), Optimal measurement of surface shortwave irradiance using current instrumentation, *J. Atmos. Oceanic Technol.*, *16*, 55–69.

Miles, N. L., J. Verlinde, and E. E. Clothiaux (2000), Cloud droplet size distributions in low-level stratiform clouds, *J. Atmos. Sci.*, *57*, 295–311.

Neale, R., and J. Slingo (2003), The Maritime Continent and its role in the global climate: A GCM study, *J. Clim.*, *16*, 834–848.

Nordeen, M. L., D. R. Doelling, P. Minnis, M. M. Khaiyer, A. D. Rapp, and L. Nguyen (2001), GMS-5 satellite-derived cloud properties over the tropical western Pacific, paper presented at 11th ARM Science Team Meeting, Dep. of Energy, Atlanta, Ga., 18 –22 March .

Qian, T. (2003), Cloud vertical structure, radiative heating profiles and diurnal variation during TOGA COARE, Ph.D. dissertation, Dep. of Mar. and Atmos. Sci., State Univ. of N. Y. at Stony Brook.

Ramsey, P. G., and D. G. Vincent (1995), Computation of vertical profiles of longwave radiative cooling over the equatorial Pacific, *J. Atmos. Sci.*, *52*, 1555–1572.

Rose, F. G., and T. P. Charlock (2002), New Fu-Liou code tested with ARM Raman lidar aerosols and CERES in pre-CALIPSO sensitivity study, paper presented at 14th Annual Conference on Atmospheric Radiation, Am. Meteorol. Soc., Ogden, Utah.

Rossow, W. B., and R. A. Schiffer (1991), ISCCP cloud data products, *Bull. Am. Meteorol. Soc.*, *72*, 2–20.

Rossow, W. B., and R. A. Schiffer (1999), Advances in understanding clouds from ISCCP, *Bull. Am. Meteorol. Soc.*, *80*, 2261–2287.

Rothman, L. S., et al. (2003), The HITRAN molecular spectroscopic database: Edition of 2000 including updates through 2001, *J. Quant. Spectrosc. Radiat. Transfer*, *82*, 5–44.

Sapucci, L. F., L. A. T. Machado, R. B. Da Silveira, G. Fisch, and J. F. G. Monico (2005), Analysis of relative humidity sensors at the WMO radiosonde intercomparison experiment in Brazil, *J. Atmos. Oceanic Technol.*, *22*, 664–678.

Shupe, M. D., P. Kollias, S. Y. Matrosov, and T. L. Schneider (2004), Deriving mixed-phase cloud properties from Doppler radar spectra, *J. Atmos. Oceanic Technol.*, *21*, 660–670.

Smirnov, A., B. N. Holden, Y. J. Kaufman, O. Dubovik, T. F. Eck, I. Slutsker, C. Pietras, and R. N. Halthore (2002), Optical properties of atmospheric aerosol in maritime environments, *J. Atmos. Sci.*, *46*, 3–19.

Sohn, B.-J. (1999), Cloud-induced infrared radiative heating and its implications for large-scale tropical circulations, *J. Atmos. Sci.*, *56*, 2657–2672.

Stith, J. L., J. A. Haggerty, A. Heymsfield, and C. A. Grainger (2004), Microphysical characteristics of tropical updrafts in clean conditions, *J. Appl. Meteorol.*, *43*, 779–794.

Tian, B., and V. Ramanathan (2002), Role of tropical clouds in surface and atmosphere energy budget, *J. Clim.*, *15*, 296–305.

Tobin, D., et al. (1999), Downwelling spectral radiance observations at the SHEBA ice station: Water vapor continuum measurements from 17 to 26 μm, *J. Geophys. Res.*, *104*, 2081–2092.

Trenberth, K. E., D. P. Stepaniak, and J. M. Caron (2002), Accuracy of atmospheric energy budgets from analyses, *J. Clim.*, *15*, 3343–3360.

Turner, D. D., B. M. Lesht, S. A. Clough, J. C. Liljegren, H. E. Revercomb, and D. C. Tobin (2003), Dry bias and variability in Vaisala RS80–H radiosondes: The ARM experience, *J. Atmos. Oceanic Technol.*, *20*, 117–132.

Wang, C. (2002), Atmospheric circulation cells associated with the El Nino-Southern Oscillation, *J. Clim.*, *15*, 399–419.

Westwater, E. R. (1993), Ground-based remote sensing of meteorological variables, in *Atmospheric Remote Sensing by Microwaves*, edited by M. A. Janssen, pp. 145–213, John Wiley, Hoboken, N. J.

Yanai, M., S. Esbensen, and J. H. Chu (1973), Determination of bulk properties of tropical cloud clusters from large-scale heat and moisture budgets, *J. Atmos. Sci.*, *30*, 611–627.

Yang, S., and E. A. Smith (2000), Vertical structure and transient behavior of convective stratiform heating in TOGA COARE from combined satellite sounding analysis, *J. Appl. Meteorol.*, *39*, 1491–1513.

Yuter, S. E., and R. A. Houze Jr. (1995), Three-dimensional kinematic and microphysical evolution of Florida cumulonimbus. Part II: Frequency distributions of vertical velocity, reflectivity, and differential reflectivity, *Mon. Weather Rev.*, *123*, 1941–1963.

Zhang, C., and M.-D. Chou (1999), Variability of water vapor, infrared radiative cooling, and atmospheric instability for deep convection in the equatorial western Pacific, *J. Atmos. Sci.*, *56*, 711–723.

Zhang, Y., W. B. Rossow, A. A. Lacis, V. Oinas, and M. I. Mischenko (2004), Calculation of radiative fluxes from the surface to top of atmosphere based on ISCCP and other global data sets: Refinement of the radiative transfer model and the input data, *J. Geophys. Res.*, *109*, D19105, doi:10.1029/2003JD004457.

Zuidema, P. (1998), The 600–800 mb minimum in tropical cloudiness observed during TOGA-COARE, *J. Atmos. Sci.*, *55*, 2220–2228.

K. L. Johnson and M. A. Miller, Brookhaven National Laboratory, Upton, NY 11973-5000, USA.

J. H. Mather and S. A. McFarlane, Pacific Northwest National Laboratory, Richland, WA 99354, USA. (jim.mather@pnl.gov)